AD743940

APPLICATIONS EVALUATION OF MATERIALS 5067 (YHG) R1

Charles S. Naiman -- Robert C. Folweiler - Paul F. Murphy
William C. Fricke - Evan P. Chicklis - John H. Hopps

SANDERS ASSOCIATES, INCORPORATED
ELECTRO-OPTICS DIVISION
95 Canal Street - Nashua, New Hampshire 03060

FINAL REPORT
Period Covered: March 1, 1970 - August 31, 1971

MARCH 13, 1972

APPLICATIONS EVALUATION OF MATERIALS
5067 (YHG) R1

Charles S. Naiman
Robert C. Folweiler
Paul F. Murphy
William C. Fricke
Evan P. Chicklis
John H. Hopps

SANDERS ASSOCIATES, INC.
Electro-Optics Division
95 Canal Street
Nashua, New Hampshire 03060

FINAL REPORT
Period Covered
March 1, 1970 - August 31, 1971

March 13, 1972

Contract Monitor: Herbert G. Lipson
Solid State Sciences Laboratory

TABLE OF CONTENTS

YHG R1

TABLE OF CONTENTS (Cont'd)

TABLE OF CONTENTS (Cont'd)

YHG R1

LIST OF FIGURES

PART I

PART II

PART III

YHG R1

DOCUMENT CONTROL DATA - R & D

(Security classification of title, body of abstract and indexing annotation must be entered when the overall report is classified)

1. ORIGINATING ACTIVITY (Corporate author)	2a. REPORT SECURITY CLASSIFICATION
Sanders Associates, Inc. Electro-Optics Division 95 Canal Street, Nashua, New Hampshire 03060	UNCLASSIFIED 2b. GROUP

3. REPORT TITLE

APPLICATIONS EVALUATION OF MATERIALS
5067 (YHG) R1

4. DESCRIPTIVE NOTES (Type of report and inclusive dates)

Scientific Final, March 1, 1970 - August 31, 1971   Approved: 24 Apr. 72

5. AUTHOR(S) (First name, middle initial, last name)

Charles S. Naiman   William C. Fricke
Robert C. Folweiler   Evan P. Chicklis
Paul F. Murphy   John H. Hopps

6. REPORT DATE	7a. TOTAL NO. OF PAGES	7b. NO. OF REFS
March 13, 1972	132	69

8a. CONTRACT OR GRANT NO	9a. ORIGINATOR'S REPORT NUMBER(S)
F19628-70-C-0220	
b. PROJECT NO. Task, Work Unit Nos. 5621-07-01	5067 (YHG) R1
c. DoD Element 61102F	9b. OTHER REPORT NO(S) (Any other numbers that may be assigned this report)
d. DoD Subelement 681301	AFCRL-72-0204

10. DISTRIBUTION STATEMENT

A - Approved for public release; distribution unlimited.

11. SUPPLEMENTARY NOTES	12. SPONSORING MILITARY ACTIVITY
TECH, OTHER	Air Force Cambridge Research Laboratories (LQ) L. G. Hanscom Field Bedford, Massachusetts 01730

13. ABSTRACT

This report covers a range of material and device development programs as outlined below.

I Evaluation of Spinel Powders as Diffuse Reflecting/Fluorescing Laser Cavity Material

This study was undertaken to improve the efficiency of Nd^{3+} doped lasers. Powders were prepared by Air Force Cambridge Research Laboratory of spinel $(MgO \cdot Al_2O_3)$ doped with Cr^{3+}. Chromium in spinel absorbs in the blue-green region and is known to fluoresce in the region of the pump bands of Nd^{3+}. The lifetime was found to be long, ~2 msec, and the fluorescent conversion efficiency low. Laser evaluation tests were performed to compare the powders, with no detectable improvement.

II Uses of GeO_2

Single crystal GeO_2 grown at AFCRL in the tetragonal form was studied for potential application as (1) electronic material for junction devices, (2) substrate for Ge devices, and (3) polarizer for optical systems.

The material as a polarizer has good potential for application because of a reasonable birefringence and longer wavelength transmission. The wide band gap of GeO_2 may permit application as a high temperature semiconductor. Additional experimentation is required to determine the usefulness. The possibility of surface reduction to form the Ge film for devices, or deposition of it by conventional techniques, should be examined.

III Medium Gain, High Energy Storage Nd^{3+} Laser Materials

A laser host with properties intermediate between Nd^{3+}:YAG and Nd^{3+}:Glass would fill the gap between these two laser hosts, thereby providing both high peak power and high average power, filling a military need in such areas as illuminators. A survey of materials indicated that some of the germanate based materials have very attractive properties.

IV Experimental Evaluation of Schottky Barrier Detectors

The Schottky barrier hot electron detectors fabricated by AFCRL were tested for their response to fast risetime pulses. The units demonstrated the fast response anticipated.

I

14	KEY WORDS	LINK A		LINK B		LINK C	
		ROLE	WT.	ROLE	WT.	ROLE	WT.
	Laser cavities						
	Diffuse reflectors						
	Doped spinel						
	Germanium dioxide						
	Neodymium lasers						
	Medium gain laser						
	High energy storage						

LIST OF FIGURES (Cont'd)

PART IV

LIST OF TABLES

LIST OF TABLES (Cont'd)

INTRODUCTION AND SUMMARY

This report covers a range of material and device development programs undertaken for Air Force Cambridge Research Laboratories and carried out by the Applied Physics Department of Sanders Associates, Inc. Electro-Optics Division. The programs are as follows:

I Evaluation of Spinel Powders as Diffuse
   Reflecting/Fluorescing Laser Cavity Material

II Uses of GeO_2

III Medium Gain, High Energy Storage
   Neodymium Laser Materials

IV Experimental Evaluation of
   Schottky Barrier Detectors

Each program is essentially independent. A description of the work and results of each are given below.

I Evaluation of Spinel Powders as Diffuse Reflecting/Fluorescing Laser Cavity Material

Laser cavities are constructed with reflectors that redirect the pump lamp radiation that misses the laser rod on one pass back toward the rod. Cavities have been constructed that use diffusely reflecting powders for this purpose, arranged as a cylinder surrounding the flash tube and laser rod. Much of the pump lamp radiation is wasted energy because it does not occur at a

wavelength that will excite the laser. It was considered possible that the wasted energy could be converted from a wavelength at which no excitation would occur, to a longer wavelength at which an excitation band occurred.

This study was undertaken to improve the efficiency of Nd^{3+} doped lasers. Powders were prepared by Air Force Cambridge Research Laboratory of spinel ($MgO \cdot Al_2O_3$) doped with Cr^{3+}, Chromium in spinel absorbs in the blue-green region and is known to fluoresce in the region of the pump bands of Nd^{3+}. Measurements were made of the fluorescence of the powders, including lifetime and fluorescent wavelength. The lifetime was found to be long, ~ 2 msec, and the fluorescent conversion efficiency low. Multiple lifetimes were observed, the normal expectation in energy transfer processes.

Laser evaluation tests were performed to compare the powders, with no detectable improvement. The long lifetime, combined with low conversion efficiency, apparently reduced the fluorescent power to less than 1% of the flashlamp power in the same wavelength region, thus not providing a measurable improvement in efficiency.

II Uses of GeO_2

The successful preparation of single crystal GeO_2 at AFCRL by a modified Kyropoulos crystal growth technique, in the

tetragonal form, led to a study of potential uses for the material. The several applications that were considered include GeO$_2$ as

Electronic material for junction devices

Substrate for Ge devices

Polarizer for optical systems.

Each area was reviewed, based on available data from various sources. In general, little data is available for the material, making hard conclusions difficult.

The material as a polarizer has good potential for application because of a reasonable birefringence and longer wavelength transmission. Present polarizer materials, typically calcite, have limitations on power density and wavelength capability, partly because it is natural material of variable quality. A source of highly controlled material is desirable for this application, which GeO$_2$ could be with further refinement and scale-up of its growth processes. Tests must be made of the material's ability to handle Q-switched laser power densities.

The wide band gap of GeO$_2$ leads to potential application as a high temperature semiconductor in the manner SiC and SnO$_2$ have been considered. Inadequate information is available to determine appropriate doping elements and resistivity ranges suitable for device fabricqtion. Additional experimentation is required to determine the required parameters and investigate

some of the ambiguities present in the available data. An outline of such a program is provided.

The other area examined pertained to use of GeO_2 as a substrate for germanium devices. The possibility of surface reduction to form the Ge film, or deposition of it by conventional techniques, should be examined. It seems probable that epitaxial films would be mechanically stable, but the electrical parameters are unpredictable. A course of critical esperiments for determining the parameters is presented.

III Medium Gain, High Energy Storage
     Nd^{3+} Laser Materials

A laser host with properties intermediate between Nd^{3+}:YAG and Nd^{3+}:Glass would fill the gap between these two laser hosts, thereby providing both high peak power and high average power, filling a military need in such areas as illuminators. This study was undertaken to compare standard materials with some of the recent data from materials under development.

High average power materials are limited by thermo-mechanical considerations such as mechanical strength, thermal expansion and thermal conductivity. Peak power is limited by spectroscopic properties such as energy storage and linewidth. The survey of materials indicated that some of the germanate based materials have very attractive properties that should be considered promptly for further development.

- 4 -

IV Experimental Evaluation of
Schottky Barrier Detectors

The Schottky barrier hot electron detectors fabricated
by AFCRL were tested for their response to fast risetime pulses
from lasers at several wavelengths in a comparison to standard
types of devices. The units, when properly matched, demon-
strated the fast response anticipated and a sensitivity compar-
able to an available InAs device at 2.06μm when the AFCRL device
was cooled to liquid N_2 temperature.

PART I

EVALUATION OF SPINEL POWDERS AS
DIFFUSE REFLECTING/FLUORESCING
LASER CAVITY MATERIAL

1.0 INTRODUCTION

This program was directed at investigating the use of Cr^{3+} doped spinel powders in the pumping cavity of Nd^{3+} glass lasers in order to improve lasing efficiency. The proposed work was a direct result of spectroscopic evaluation of Cr^{3+}/Mn^{2+} doped spinel crystals performed jointly[1,2] by AFCRL and Sanders' personnel.

Cr^{3+} spinel powders were prepared at AFCRL. Reflectivity and fluorescence measurements of the powders were made at AFCRL; pulsed fluorescence measurements and laser evaluation of the powders were performed at Sanders Associates. To gauge the effectiveness of the concept, lasing efficiency measurements were made with undoped and Cr^{3+} doped spinel powders. For Nd^{3+} glass operation, no measureable improvement in lasing performance was observed which could be attributed to the use of fluoresing powders under the conditions employed in these tests. Spectroscopic and laser studies are reported in detail below.

2.0 SPECTROSCOPY OF Cr^{3+} DOPED SPINEL POWDERS

Flame fusion spinel powders, undoped and doped with 1% Cr^{3+}, nominal, were prepared with $MgO:A\ell_2O_3$ ratios of 1:1, 1:2, 1:3, and 1:4 at AFCRL. Fluorescence spectra (AFCRL) of the powders were similar to that observed[3,4] with single crystal Cr^{3+} doped spinel (Figure 1). Diffuse reflectance spectra of the powders taken with a Cary 14 (AFCRL) showed fairly uniform reflectivity ∼ 60% throughout most of visible region of the spectrum except for small dips due to the Cr^{3+} absorption bands.

Figure 2 shows the characteristic absorption bands of Cr^{3+} spinel single crystals in good agreement with the results of a number of investigators[3-6] and show splitting of the blue and green absorption peaks at ∼ 25 x 10^3 and 18 x 10^3 cm^{-1} respectively as the ratio of alumina is increased. This effect has been the subject of a number of interpretations [1,3,4] including trigonal distortion at the Cr^{3+} site and the existence of two sites (octahedral) for the Cr^{3+}. X-ray data have not revealed the presence of a second phase in the spinel ruling out Cr^{3+} in $A\ell_2O_3$ or MgO.

Fluorescence spectra of the powders taken at room temperature (AFCRL) were characteristic of the emission properties of Cr^{3+} in single crystals of the spinel structure. In nearly stoichiometric samples the fluorescence is characterized by a single no phonon R-line with satellite vibronic structure which, at room temperature, appears at the high and low energy side of the R-line. In addition, the spectrum is complicated by the presence of N-lines which appear to be the result of pair (Cr^{3+})

states[3]. As the alumina ratio is increased in synthetic spinel
the emission is characterized[3] by the appearance of a broad fluores-
ence band in the 9000 - 14,000 cm^{-1} region. The band fluorescence is
not unlike the fluorescence spectrum of Cr^{3+} in MgO observed by Parker[9].

2.1 Lifetime Measurements

The details of the pulsed fluorescence apparatus are described in
references 7 and 8. Early data were taken under broad band pulsed
illumination. The fluorescence decay which followed the flashlamp pump-
ing was not simply exponential in any of the regions detected. Moreover,
the observed lifetimes were found to vary depending upon the pumping con-
ditions; under broad-band illumination, all components of the emission
(the R-line and the IR band) exhibited long lived decay components.

Excitation spectra (AFCRL) for the "R" line and band fluorescence
in the off stoichiometric samples were critically dependent on the fluor-
escence band detected; that is, the "R" line and band fluorescence ex-
hibited different excitation spectra. This data combined with prelim-
inary lifetime measurements, indicated support for the "two site" model
described in reference 1.

Cr^{3+} doped stoichiometric spinel shows many of the features of the
ruby spectrum. However, as the ratio of alumina is increased, it appears
that a second site is formed in the material under the influence of a
different crystal field. This site is occupied by either $A\ell^{+3}$ or Cr^{+3}.
The features of this second site appear to be similar to that of Cr^{3+} in

MgO[9] in that the R line fluorescence and an emission band to the red of the R line is observed. The band fluorescence appears to be Stokes shifted emission from the $^4T_2$ state.

The gross features of the emission spectra are complicated by the apparent observation of energy transfer between the two sites as revealed by excitation spectra and lifetime measurements.

The following diagram illustrates the manner in which such a two site model can be used to explain the experimental data:
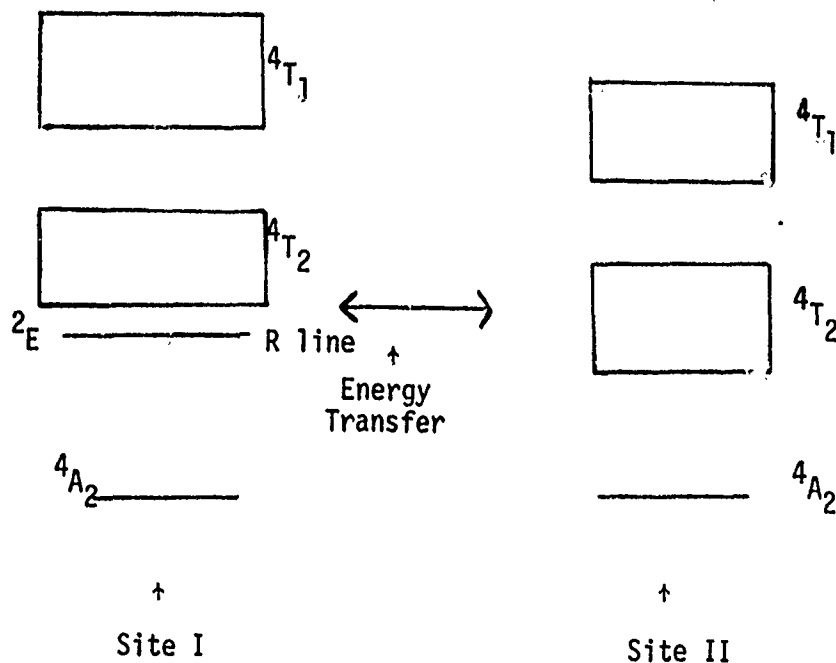
In stoichiometric spinel only site I is observed. Interpretation of the absorption spectrum follows straightforwardly from the energy level diagram. The fluorescence spectrum is somewhat more complicated by the existence of "N" line spectra which are not accounted for in this model. The main features of the fluorescence spectra, however, fit this construct. The no-phonon R line emission at room temperature is the result of absorption of pump radiation in the $^4T_1$ and $^4T_2$ states with subsequent non-radiative decay to the ^2E metastable state from which fluorescence occurs. At room temperature splitting of the ^2E state is not observed. At 77°K two R lines are resolved[3]. The symmetrically placed lines on the high and low energy side of the no phonon line can be explained as a harmonic modulation of the crystal field (Dq) due to lattice vibrations. Thus the Cr^{3+} ions are in effect placed in a harmonically varying field and the Cr^{3+} energy levels are correspondingly frequency modulated.

The lifetimes of the emitting states in the stoichiometric spinel at room temperature under broad band illumination could not be characterized by a single decay rate. Wood et al[3] observed a 36.5ms lifetime for the R line and ~ 13ms lifetime for the N lines at 77°K. Our room temperature observation of multiple decay rates for the R line fluorescence at room temperature points to the possibility of energy transfer between the N states and the R line in these heavily doped (1%) powders. The R line decay was not simply exponential but can be fitted with 9 and 24ms rates. The N line emission was insufficiently sharp at room temperature in the 1% doped powder samples to permit accurate measurement of the lifetime.

Off Stoichiometric Spinel

As the composition of the material is altered with the introduction of more Al_2O_3 into the lattice, a second octahedral site[1] is formed and the complex emission and absorption spectra observed can be explained as the composite absorption and fluorescence properties of Cr^{3+} in both sites.

The continuous fluorescence of Cr^{3+} spinel is characterized by the growth of the IR band to the red of the R lines as more Al_2O_3 is introduced into the lattice. The lifetime of the R line under broad band illumination (excitation pulsewidth ~ 600μs) decreases as excess alumina is introduced. All the emission bands observed under these conditions were multiply exponential and the fits made to the observed decay may not be unique.

The observed rates varied from 9, 24ms in 1:1 spinel to 0.9 and 3.8ns in 1:4 for the R line emission. The similarity of the rates observed in other regions of the spectrum seemed to contradict the proposed two site model. Further experiments were felt to be in order.

Since the observation of the same lifetimes (within experimental error) of the R line and band emission could be accounted for by assuming a one site model or energy transfer between two sites, it was decided to test this hypothesis by resonant pumping the resolved absorption bands of site I and II and observing the time dependence of the emission. Figures 3 and 4 show the excitation spectra for the R line and band emission of a 1:325 ($MgO:Al_2O_3$) spinel crystal with 0.37% Cr^{3+} taken at AFCRL. The 5500 and 4000Å peaks are assigned to the (R line) site I and the 6200 and 4800Å peaks to the site II (band fluorescence).

Pulsed fluorescence measurements were made with a ~ 10μs flashlamp duration and appropriate filters to isolate regions of the exciting radiation and fluorescence. The results are summarized in the table below. Numerical values were assigned to the decays only if a reasonable fit could be made over a time duration of at least two time constants. In many instances this was not possible since sufficient signal/noise was not available in the tail of the decay.

YHG P1

PULSED FLUORESCENCE DATA FOR 1% Cr^{3+} SPINEL
POWDERS - FLASHLAMP DURATION 10μs

Sample	Pump Band	Detected Fluorescence	Measured Rate
1:1	(6400) Site II	Site II (7800Å)	Not observed
1:2	(6400)	Site II	45 ± 15μs
1:3	(6400)	Site II	45 ± 15μs
1:4	(6400)	Site II	45 ± 15μs
1:1	(4660Å) Site II	Site I (6952Å)	Not observed
1:3	(6400)	Site I	Not observed
1:2	(4660Å) Site II	Site II (7800Å)	100μs + slower component
1:3	(4660Å)	Site II	100μs + slower component
1:4	(4660Å)	Site II	100μs + slower component
1:1	(5300Å) Site I	Site I (6952Å)	9.6ms
1:2	(5300Å)	Site II (7800Å)	100μs + slower component
1:2	(5300Å)	Site I	multiple
1:3	(5300Å)	Site I	Fast component + 3ms
1:3	(5300Å)	Site II	multiple
1:4	(5300Å)	Site I	multiple
1:4	(5300Å)	Site II	150μs
1:1	Broad band	Site I (6952Å)	100μs + slower component
1:4	Broad band	Site I	multiple

Extreme care must be exercised in interpreting these results as the measured rates are not necessarily the actual fluorescent lifetimes. Rather, the decay of the emission in some instances is the superposition of decay and buildup modes and some of the measured fits may be ambiguous. The pulsed fluorescence data, excitation, absorption, and fluorescence spectra are in good agreement with the two site model.

The emission from the site I (stoichiometric Cr^{3+} doped spinel) is characterized by the R line emission and its associated vibronics. Emission from the $^4T_2$ is not observed at room temperature due to rapid non-radiative decay to the ^2E state. Emission from the $^4T_2$ in ruby and emerald has been observed[10] by observing the fluorescence at sufficiently high temperature to maintain an equilibrium population in that state. Thus the site I is "ruby like" in its emission properties with a longer lifetime for the R line emission and a much smaller trigonal field splitting of the ^2E state (R line splitting ~ 6 cm^{-1}).

The broad band fluorescence which appears in off stoichiometric samples is assigned to Stokes shifted emission from the $^4T_2$ state in the second site. Lifetime data are complicated by the observation of energy transfer between the two sites. However, by resonant pumping the $^4T_2$ band of the site II, we have observed lifetimes for the $^4T_2$ emission of approximately 50μs <u>independent</u> (within experimental error) of the $MgO:A\ell_2O_3$ <u>ratio</u>. This result provides strong evidence for the two site model: as excess $A\ell_2O_3$ is added to the lattice, an increasing number of octahedral sites (site II) become available with lower trigonal distortion than the site I and weaker Dq. Thus the growth of the IR band (Stokes shifted emission from the B site) as the ratio of alumina is increased is attributed to the increasing number of Cr^{3+} ions in this site.

YHG R1

3.0 SPINEL POWDERS IN A DIFFUSE REFLECTING/ FLUORESCING LASER CAVITY

Because the emission spectra of off-stoichiometric Cr^{3+} doped spinel powders overlaps the absorption (and excitation) spectra of Nd^{3+} doped glass laser materials, an attempt was made to increase the pumping efficiency of Xe pumped Nd^{3+} glass laser rods with the use of the powders as a diffuse reflecting/fluorescing laser cavity.

The absorption spectrum of the laser material shown in Fig. 5 is to be compared to the emission spectrum of Cr^{3+} spinel in Fig. 1

Laser Measurements

An American Optical NS-0835 Nd glass rod was purchased under the contract. The rod was 1/4 x 3" and preliminary laser tests were performed in an MgO cavity with adequate provision for cooling. Considerable mounting difficulties were encountered with the rod; in the initial configuration the rod was held with metal holders in an "0" ring seal. Very high thresholds for Nd operation (600 Joules) were observed and this anomaly was traced to insecure mechanical mounting - the mechanical shock wave generated by firing the flashlamp was sufficiently intense to move the rod faces out of alignment. With improved metal holders and an epoxy seal, threshold was reduced to ~ 60 Joules with slope efficiency of ~ 1% in the MgO cavity.

To avoid mounting problems altogether, a new approach was formulated. A number of cavities were constructed by mounting two Vycor tubes coaxislly with sufficient space between to pack the powders. The inside diameter of the cavity was 0.75" with the flashlamp providing support for the whole arrangement and the rod sitting unattached at the bottom.
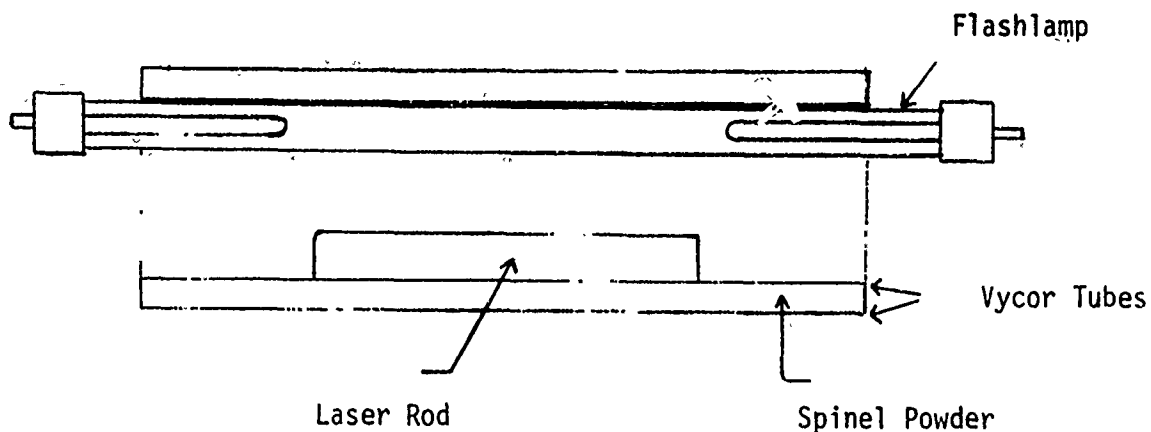
Using this configuration low thresholds for Nd operation were observed:

Nd Glass Results

The parameters of the Nd glass test are as follows:

              Rod: American Optical Type NS-0835
        Flashlamp: EG&G FX-42.3
       Pulsewidth: 1ms
  Coupling Mirrors: 99.9% R rear, 65% R front
        Detection: TRG energy meter, RCA 925(S-1) photodiode
  Band Parameters: C = 375μf, L = 300μH

The threshold for oscillation and slope efficiency for Nd operation
was 50 Joules and 1.3% respectively with the 1% Cr^{3+} 1:3 spinel powder
as the cavity reflecting material.

With the undoped 1:3 powder the threshold was 45 Joules with a 1.3%
slope efficiency. The operating conditions were as identical as possible
between the two tests; the estimated uncertainty in our measurements
is $\pm$ 10%. Thus no improvement in Nd^{3+} lasing efficiency as a result of

the use of Cr^{3+} doped spinel powders was observed under the conditions employed in these tests. The apparent improvement in efficiency over that observed in a MgO cavity (1% slope efficiency) is probably the result of closer optical coupling employed in the spinel powder cavities.

SUMMARY AND RECOMMENDATIONS

Perhaps the most sensitive parameter which was not carefully studied was the effect of particle size on the ration of scattered to fluorescent light. For the powders fabricated for these tests (100 micron mesh) the ratio of scattered to fluorescent intensity in the center of the emission band of the Cr^{3+} was at least 100:1. Consequently the increase in the energy density in the cavity of radiation resonant with the absorption bands of the Nd laser material was not substantially increased with the Cr^{3+} doped powders.

A number of variables control the ratio of fluorescence to scattered light and should be investigated.

A. Particle Size

A study of scattering cross section vs. particle size was beyond the scope of this contract. A number of authors[12-14] discuss the problems with the intent of determining the optimum particle size for maximum reflectivity. The requirements for the diffuse reflecting/fluorescing cavity material are somewhat different as:

a) the absorption of the pump radiation in the fluorescence excitation bands of the spinel must be maximized (to increase the fluorescence output) and

b) the reflectivity in other spectral regions must not be seriously degraded.

Minimizing the scattering from the powders would satisfy the first requirement and could be accomplished with larger individual crystallites with an index matching fluid between the flashlamp and the powder. In such a configuration the powders would be nearly transparent.

To satisfy (b) above a specularly reflecting material (silver wrap or an aluminized tube) could be employed as the outer annulus of the cavity.

B. Alternative Cavity Configuration

Spinel may be hot pressed into transparent cylinders permitting the use of a cladding technique similar to that employed with considerable increased pumping efficiency of Nd glass laser rods. Such an approach may, however, lead to severe fabrication problems as the cladding must make optical contact with the rod. Alternatively, the spinel might be formed into a larger cylinder providing the annulus for the cavity backed by a high reflectivity coating. Both these approaches minimize the scattered light and maximize the absorption, hence fluorescence for fixed Cr^{3+} concentration.

C. Alternate Pumping Techniques.

Swedish workers have reported increases of 1.5 -3 [15] in the visible output of Xe discharges through the use of fluorescent converters. A variety of substances were evaluated using very high input energies to the flashlamp in short flashlamp pulses. The converter solutions had high absorption in the uv (the peak of the flahlamp discharge) and emission bands in various regions of the visible.

The configuration employed examined the spectral center transmitted through the converter solution. The effectiveness of this scheme appears to be the result of high fluorescence efficiency in the converter, low

scattering cross section of the solutions, and very high dis-
charge current into the flashlamp with concommitant shift of
the emission to the ultra-violet where the converter solutions
strongly absorb. Unfortunately, such high current discharges
could not be employed in the spinel powder tests as damage to
the laser rods would certainly have resulted.

In summary, improved pumping efficiency of Nd glass laser
rods as a result of the Cr^{3+} fluorescence in off stoichiometric
spinel powders has not been observed. This is attributed to the
high ratio of scattered to fluorescence radiation in the cavity.
On average, the scattered flashlamp radiation density in the
Cr^{3+} fluorescence wavelength band was ~ 100 x greater than the
energy density due to fluorescence. This condition might be
drastically improved by the use of a configuration in which the
scattered radiation is minimized and the fluorescence amplitude
maximized. In view of the known improvement of laser pumping
efficiency via fluorescence and reabsorption in clad laser rods,
and the increased visible radiation obtained from Xe pumped
fluorescence converter solutions[15] enhanced pumping efficiency
of Nd lasers as a result of absorption and re-radiation in Cr^{3+}
doped spinels seems feasible in an improved configuration.

PART I

REFERENCES

1. E. Farrell et al, "The Optical, Fluorescent and Physical Properties of Flame Fusion Spinel", presented at the International Confer. on Crystal Growth, Birmingham, England July 1968.

2. C. A. Pitha, J. Adamski and C. S. Naiman, "Site Preference for Manganese in Flame Fusion Spinel", 20th Mid-America Symposium on Spectroscopy, Chicago 1969.

3. D.L. Wood et al, J. Chem. Phys. 48, No. 11 (1968).

4. R. A. Ford and O. F. Hill, Spectrochim. Acta 16, 1318 (1960).

5. R. H. Arlett, J. Am. Ceramic Soc. 45, No. 11 (1962).

6. V. I. Cherepanov and A. N. Mew, Soviet Phys-Solid State 6 No. 7 (1965).

7. Quarterly Progress Report #1 (Contract #F19528-70-C-0220)

8. Quarterly Progress Report #10 (Contract #F19628-68-C-0162)

9. J. H. Parker et al, in "Optical Properties of Ions in Crystals" Ed. by Crosswhite & Moos p 251, Interscience, N.Y. (1967).

10. P. Kisliuk and C. A. Moore, Phys. Rev. 160, No. 2 (1967).

11. C. F. Pappard and H. A. Lee, "Energy Transfer Kinetics in Erbium Glass Lasers", Laser Journal, May/June (1970).

12. J. R. Aronson et al, Applied Optics 8, No. 6 (1969).

13. N. T. Melamed, J. Applied Phys. 34, No. 3 (1963).

14. E. A. Schatz, JOSA 56, No. 3 (1966).

15. S. Claesson and W. Wladimiroff, "Stable Fluorescent Converter Solutions Enhancing Optical Pumping Efficiency in the Visible Region", Final Report Contract No. 4654(00) Inst. of Physical Chemistry, U. of Uppsala, Uppsala, Sweden (1966).

Fig. 1: Fluorescence Spectra of $MgO:A\ell_2O_3$ 1% Cr^{3+} Powders

1:3

1:1

$MgO:A\ell_2O_3$

1% Cr^{3+}

[From H: Lipson, AFCRL]

WAVELENGTH Å

Relative Fluorescence Amplitude

10,000

9000

8000

7000

10

8

6

4

2

R1-1

YHG R1
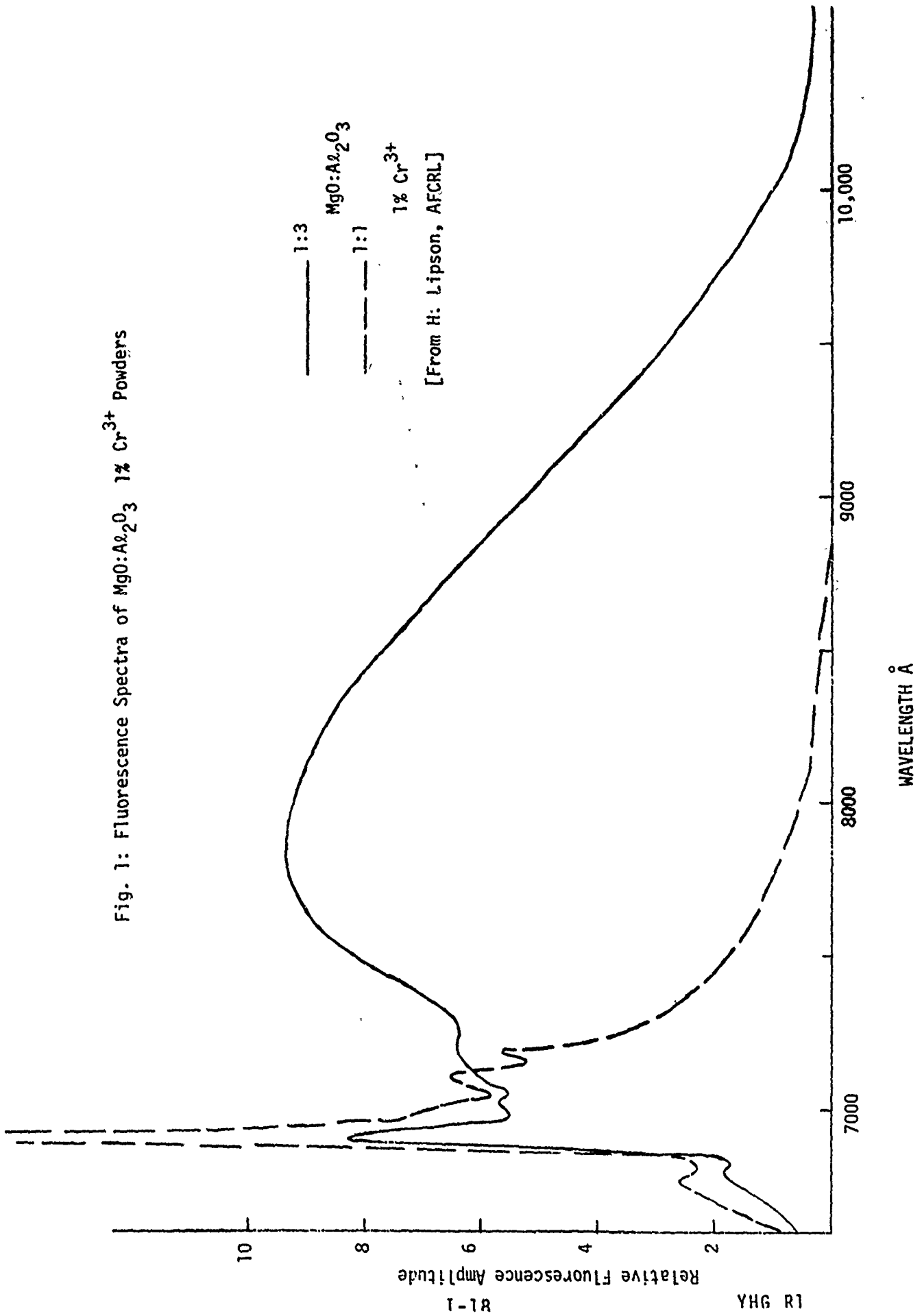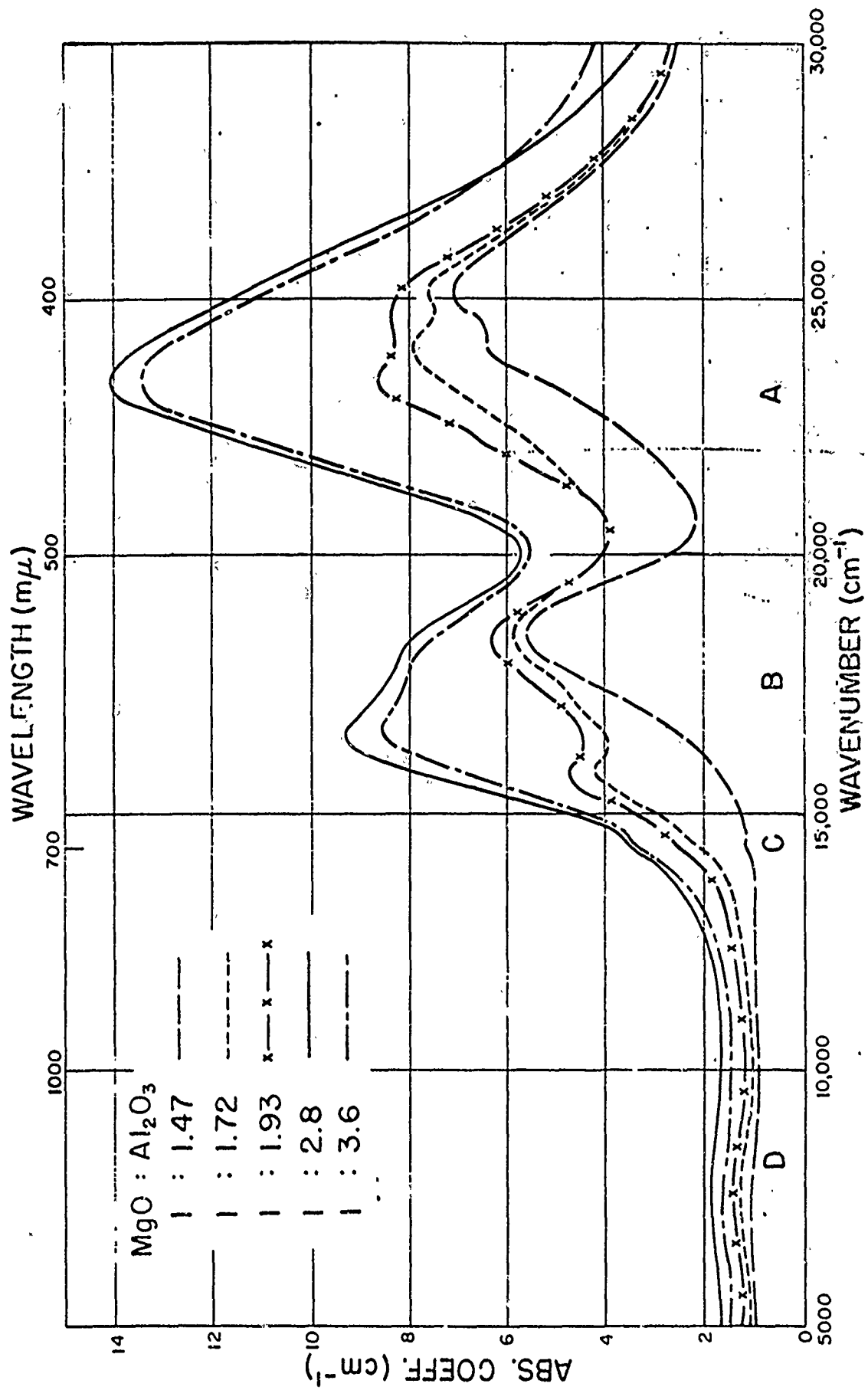
Fig. 2: Absorption spectra of Cr-doped MgO:Al₂O₃ solid solution series.

WAVELENGTH (mμ)

WAVENUMBER (cm⁻¹)

ABS. COEFF. (cm⁻¹)

MgO : Al₂O₃
1 : 1.47
1 : 1.72
1 : 1.93
1 : 2.8
1 : 3.6

Fig. 3: R Line Fluorescence Excitation Spectrum of 1:3.25 Spinel, 0.37% Cr^{3+} Sample #397-8 Detector set at 6920Å

02-1
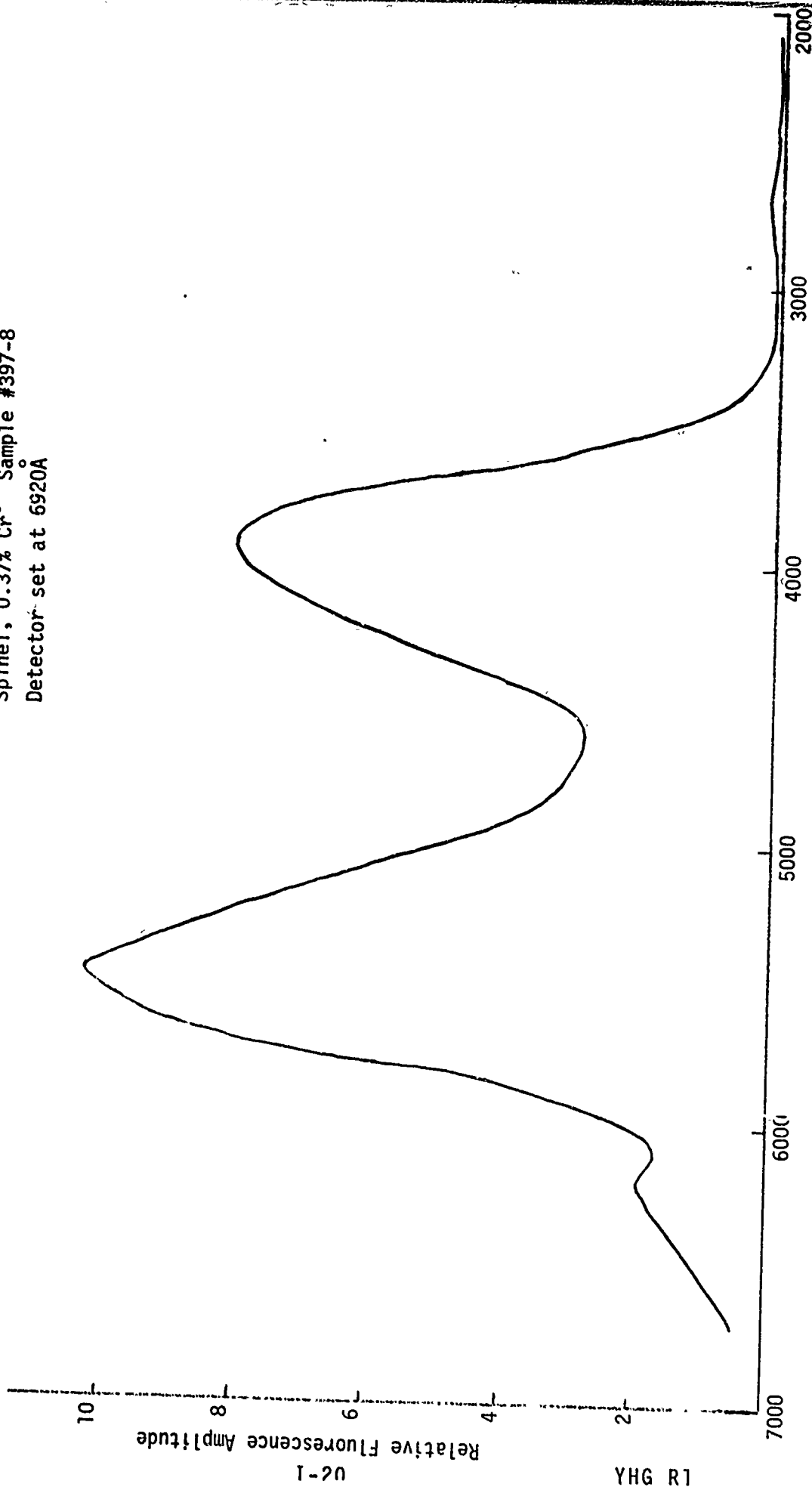
YHG R1

Fig. 4: Band Emission Fluorescence Excitation
Spectrum of 1:3.25, 0.37% Cr³⁺ Spinel
Sample #397-8
Detector set at 7900Å

Exciting Wavelength Å

Relative Fluorescence Amplitude

YHG R1

I-21
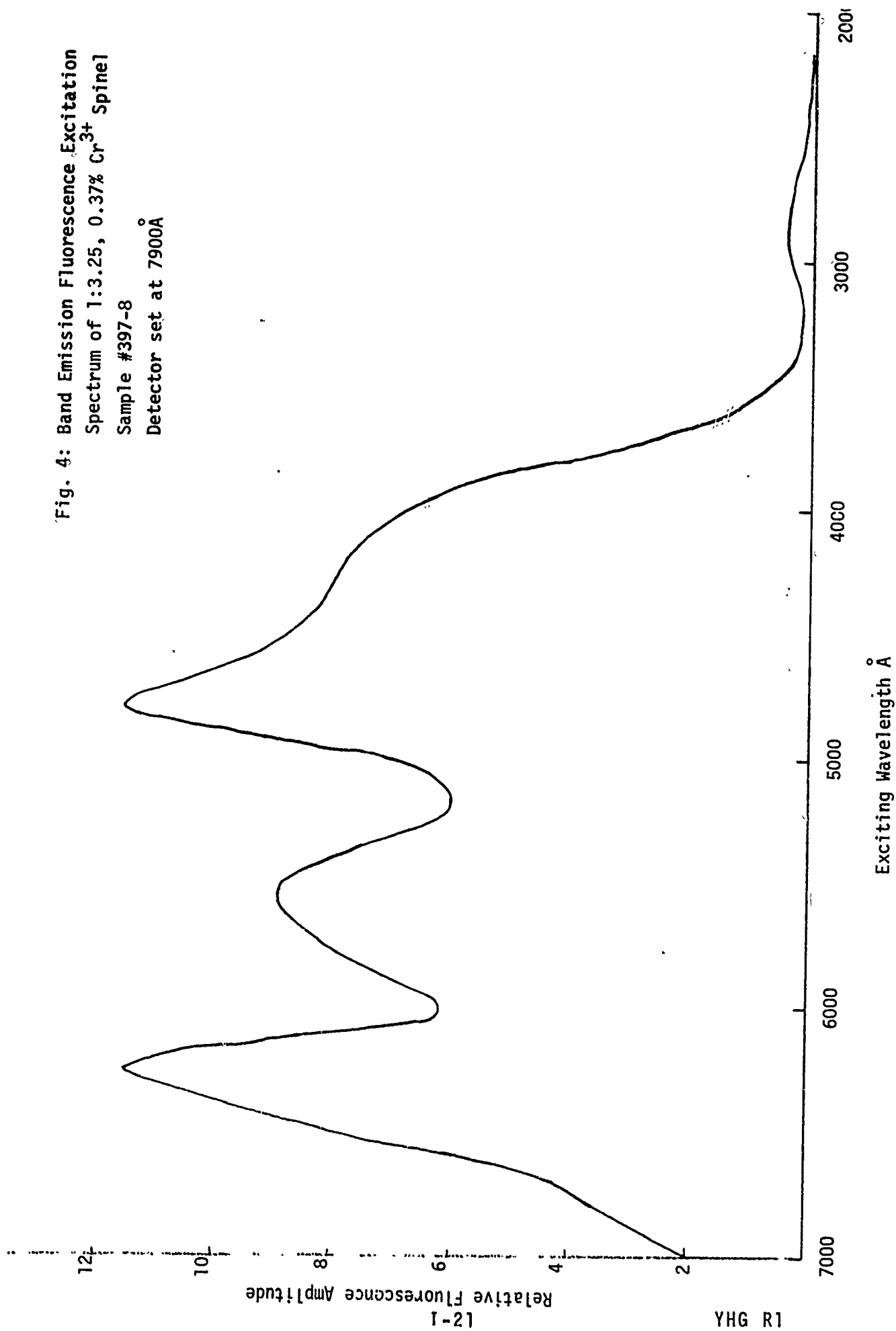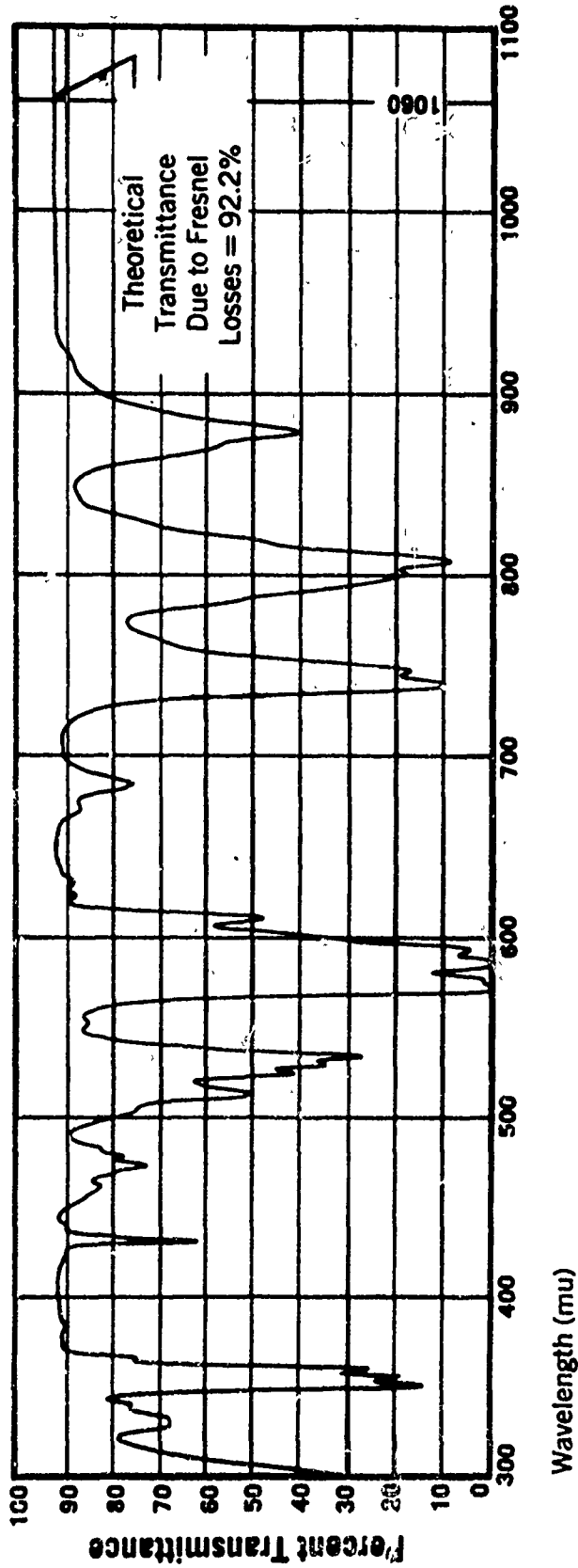
Figure 5: Representative curve of absorption spectrum for NS Series and NR Series glass types. (Sample: 5mm thick #0835 glass.)

PART II

SPECIAL STUDY ON USES OF GeO_2

1.0 INTRODUCTION

The recent availability of tetragonal GeO_2 single crystals[1], grown by a top-seeded flux technique at AFCRL, has led to an interest in potential uses for the material. There are several applications worth pursuing that we consider in this report. The ones that are discussed here include applications as

        Electronic Material
           - for junction devices

        Substrate
           - for germanium devices

        Polarizer
           - for optical systems.

Each are presented, and the known properties used to judge the potential as far as possible.

2.0 GeO_2 AS AN ELECTRONIC MATERIAL

2.1 Introduction

The electrical properties of germanium dioxide, GeO_2, are essentially unknown. It is important to know these properties, however, for applications of GeO_2 whether this information may simply influence the incorporation of GeO_2 passively in a particular application, may enhance the usefulness of GeO_2 in a particular electronic context, or may be the primary reason that GeO_2 is the best choice for a particular application.

Evaluating GeO_2 electrically is a straightforward, relatively easy task once, as is now the case, a source of good single crystals is available. We consider this evaluation in detail below. Of interest will be the determination of basic conduction parameters of GeO_2 so that in turn we may consider in a more direct manner the potential usefulness of GeO_2 in both active (devices) and passive (substrates) electronic applications. GeO_2 is known to have a wide band-gap and this immediately makes it of interest for use at high temperatures. If it is shown to be a semiconductor that can be doped to low resistivities it would also be an important transparent electrode and be useful to higher energies (5.5 eV) than the commonly used SnO_2 (3.5 eV).

A great deal of effort has been expended developing semiconductor materials that can be useful to 400-500°C. Si transistors useful to 200°C have been made and it was earlier hoped that GaAs might be useful in high temperature transistors. The most thoroughly explored material for high temperature applications is SiC[2] and recently stannic oxide[3] has shown

II-2   YHG R1

promise as a high temperature semiconductor. Still the need for new

materials exists and is very real. There are several properties that a

material must have if it is to be useful as a high temperature semi-

conductor. First, it must have a wide band-gap, as GeO_2 does, so that

thermal excitation of carriers across the gap is negligible at the temper-

atures of interest. Second, it must have good high temperature stability.

For electronic applications this also means microscopic stability of the

doping and other impurity atoms in the crystal lattice. Thirdly, it

should have the ability of being doped with electronically active dopants

and of being so doped efficiently, that is, without a large number of

unionized dopant atoms or high compensation. Finally, the carrier mobil-

ities should be high, certainly well over 10 cm^2/V-sec, so that low re-

sistivities (0.1 - 10 Ω-cm) can be achieved at moderate doping levels

(10^{15} - 10^{17} cm^{-3}). For comparison, stannic oxide[3], SnO_2, can only be

made n-type but is easily doped and has an electron mobility of

250 cm^2 V-sec at 300°K. (SnO_2 is a relatively new entry into this area

and is still under study.) Silicon carbide[2], on the other hand, can be

made both n- and p-type and has electron mobilities of > 1000 cm^2/V-sec

at 300°K (crystal growth and quality, however, are not well controlled

in the SiC system).

This section will be concerned with a discussion of the presently

known parameters of GeO_2, and an extension of these parameters to potential

device construction.

2.2 Present Knowledge

As we have mentioned previously, the existing knowledge of GeO_2, particularly as concerns its electrical properties, is very limited. The few experiments already performed at AFCRL[1] on the recently grown crystals represent a substantial portion of the known work on GeO_2 crystals. Germanium oxide is known to be a semiconductor with a band-gap of over 5.5 eV[4]. Resistivity measurements of GeO_2 films formed on germanium by oxidation have been reported by Zwerdling and Sheff[5] and by Wales[6]. These authors list, respectively, resistivities of 10^{10} Ω-cm and 3×10^{12} Ω-cm for their films. In both cases the films had the tetragonal structure of GeO_2 and were not intentionally doped with any electronically active impurities. The only measurement of resistivity on a single crystal was made by Papazian[7] on a hexagonal GeO_2 crystal. He measured $>10^{15}$ Ω-cm at room temperature and $> 5 \times 10^{10}$ Ω-cm at 400°C, also on undoped crystals.

The static dielectric constant was measured at AFCRL[1] to be $76.0_{\parallel} c$ and $28.0_{\perp} c$. It has been estimated by Wales[6] from measurements on thin films, however, to be 6.4 at 1 kHz. It is interesting to note that the dielectric constant of stannic oxide, SnO_2, which also has the rutile structure, was long thought[8] to be $24_{\parallel} c$ and $23.4_{\perp} c$ and only recently has been shown[9] to in fact be $14_{\parallel} c$ and $9_{\perp} c$. The error arose because of the presence of water in the originally studied natural SnO_2 crystals.

The energy band calculation of F. J. Arlinghaus and W. A. Albers, Jr.[10] shows that the conduction band effective masses are $0.4 m_{e\perp} c$ and $0.6 m_{e\parallel} c$.

These masses and the wide band-gap imply that acoustic deformation potential scattering[11] will be important in GeO_2. This scattering mechanism mobility varies as $m^{-5/2}$. It also varies inversely with the square of the deformation potential for dilating strain for the conduction band, also expected to be large in GeO_2. Also, Ladd[12] from a calculation of the crystal energies in GeO_2, concludes that the M-O bonds have a strongly ionic character and so the crystal will be quite polar. (The dielectric constant measurements support this conclusion.) Thus, the mobility is expected to be limited by polar optical mode scattering. A final contribution causing lowering of the mobility will, of course, be impurity scattering. This, however, can potentially be eliminated as crystal quality improves. Neglecting this, then, a crude estimate indicates that the electron mobility in GeO_2 will not be high, of order 10^2, at best.

The presently known information is inadequate to adequately predict the range of properties necessary. As we will discuss now, however, it is an easy and straightforward matter to experimentally learn a great deal about GeO_2; and from that basis, in fact only from such a basis, can GeO_2 be realistically evaluated.

2.3 Pertinent Experimentation

The most relevant electrical measurements to be made on GeO_2 are of the bulk resistivity, mobility, and carrier concentration of single crystals. The basic questions to ask are, one, how good an insulator is "pure" tetragonal GeO_2; two, can electronically active impurities be added to GeO_2 to make it a low resistivity semiconductor; and, three, if active impurities

do exist, what are the detailed electronic properties of such "doped" crystals? The answers to such questions should be straightforwardly obtainable and are important to evaluating germanium oxide's potential for electronic applications; in fact, for all applications.

2.3.1 Undoped Crystals

The term "undoped crystals" is used to mean the purest crystals obtainable and thus depends on the crystal growth technique. The important point is that no electronically active impurities have been intentionally added to the crystals. The crystals presently under consideration, i.e., the GeO_2 grown at AFCRL, are in this category.

The parameter of interest in undoped crystals is their resistivity. This is anticipated to be quite high; in such a case, mobility and carrier concentration are both difficult to measure and of little practical use. The resistivity, however, is important to know, particularly if the GeO_2 is to be used as a substrate for low resistance Ge layers. An initial indication of the magnitude of the resistivity should be obtainable from the same experiment utilized to measure ϵ in these crystals. It is simply obtained from the lossy, or resistive, component of the net sample impedance. An accurate two terminal resistivity measurement, however, requires that ohmic, low resistance contacts be made to the sample. These are likely to be both difficult to achieve and to evaluate. A better technique would be one in which no contacts were employed, such as one in which the GeO_2 is used as the dielectric in a waveguide cavity[13]. The other possibility would be a four-terminal resistivity measurement performed using a bar-shaped sample

with current contacts at either end and two voltage probes along the length alone[14]. This will require a high input impedance voltmeter.

It would be instructive, whichever type of measurement is made - this decision of course depends both on the magnitude of the resistivity and on the available equipment - to consider the dependence of the resistivity on temperature and measurement frequency. These dependences are not immediately obvious, but are easy to obtain a feel for and are important again for substrate applications of GeO_2. Measurements at only three temperatures and frequencies would be sufficient to indicate what more, if anything, should be done.

2.3.2 Doped Crystals

It is important to determine if GeO_2 crystals can be doped with electronically active impurities and thus be made into a useful semiconductor. To do this, attempts should be made to grow crystals containing small percentages of group III - Aℓ, Ga, In - and group V - Sb, As, P - elements. While electronically useful concentration levels are 10^{14} to 10^{17} atoms/cm^3, melt dopings corresponding to 10^{18} to 10^{19} atoms/cm^3 (0.001 to 0.01%) are acceptable in the initial feasibility investigations. A first choice might be Sb, a known n-type dopant in SnO_2[3].

Once it is determined that these impurities can be successfully introduced into the crystals, it must be determined what effect they have on the electrical properties of the GeO_2. Again the initial measurement should be

of resistivity, and this can be very crude. It need only be sophisticated enough to tell if the resistivity has been significantly lowered. A con-centration of 10^{14} cm^{-3} and a mobility of 1 cm^2/V-sec corresponds to a re-sistivity of 10^5 Ω-cm. If the measured resistivity was higher than this, it would indicate that GeO$_2$ is likely to not be a useful electronic semi-conductor, as it would be difficult to dope and have rather low mobility. If the measured resistivity was lower than this, it is next important to determine the mobility and carrier concentration. The pertinent measure-ments are of the Hall effect[15] and resistivity as a function of temper-ature. From these measurements the mobility and the main carrier scatter-ing mechanisms can be determined. The net donor and acceptor concentra-tions and the donor (or acceptor, in p-type material) ionization energies can also be calculated. It should be noted that while the Hall effect is isotropic[16], the mobility will not be, and samples oriented with respect to the current should be used.

The donor concentration calculated from these measurements should be compared with the donor element concentration determined spectrochemically or by some comparable technique. Agreement between these two figurse would show that all the dopant atoms are electronically active, a very desirable situation as any inactive atoms only serve to interfere with conduction, i.e., to lower the mobility. The best donor, or acceptor, do-pant, in general, is the one which is most easily introduced into the crystals and which enters the crystals in such a manner that all of the atoms are electronically active. The mobility data and its analysis can yield

information on the crystal purity and perfection also. It will be possible to determine from it the extent to which the mobility is limited by the lattice, an intrinsic limitation, and how much by impurities, an extrinsic and surmountable limitation.

With this information the first realistic considerations can be given to device potentials of GeO_2. If the situation is encouraging, i.e. μ of order 10^2, easily doped in 10^{14} to 10^{17} cm^{-3} range, a next step would be the fabrication of Schottky barrier diodes[17] on GeO_2. These devices, in addition to being themselves useful as diodes and as gates in FET geometries, will give information on surface barriers and contacts both ohmic and rectifying, and on the net donor concentration. This last information is obtained from measuring the barrier small signal capacitance as a function of applied bias[17]. It can be used to determine the donor homogeneity in a slice if many small devices are formed across the sample, and to determine if shallow trapping is a problem by comparing this concentration with that determined by Hall measurements.

It is often stated that almost any metal evaporated on a semiconductor surface will create a rectifying Schottky barrier[17]. This is often an oversimplification unless care is taken in preparing the semiconductor surface. A polished surface should be used. It has been found, in Si and other semiconductors, that polishing creates surface damage extending into the crystal up to 10 times the grit size, so a careful polish should be done and then the surface should be chemically etched to remove surface damage due to the polish. If a reducing etch is necessary, this should be

followed by an oxidizing etch to return the surface to a good GeO_2 surface. Then the barrier metal can be evaporated on the surface through a mask - aluminum foil with pinholes ~ 20 mil in diameter is sufficient. Good barrier metals are Au or Pt as they have large work functions. They should be evaporated in a vacuum < 10^{-6} torr and slowly. To evaluate the barriers a transistor curve tracer is useful. Once good rectifying characteristics are obtained, capacitance-bias voltage measurements and calculations of net donor concentrations can be made.

YHG R1

3.0 GeO_2 AS A SUBSTRATE FOR Ge SEMICONDUCTORS

3.1 Introduction

The possibility of producing epitaxial layers of Ge on GeO_2 by simply reducing the GeO_2 surface or depositing Ge on the surface is an interesting one. As is the case with GeO_2 itself, there are some straightforward electrical characterizations which must be made on such Ge layers, characterizations which are essential to evaluating the usefulness of the layers. It should again be emphasized that information on the electrical characteristics of GeO_2 is important to have for these experiments as it is the substrate and is intimately involved in any measurements made on the Ge layers. Ideally it will be insulating for the purposes of these experiments but the validity of such an assumption must ultimately be known. In this context it should also be noted that the Ge will be doped and thus the behavior of the dopant atoms in GeO_2 is important to have determined at some point early in the study.

3.2 Requirements for Substrates

3.2.1 General Criteria

The criteria for any material to be a successful substrate are:

(a) The crystal substrate should have a comparable crystal structure to the deposited layer. The degree to which the structures are not comparable is called the "misfit" of the structures.

(b)   The substrate must be chemically stable. It cannot dissolve appreciably in the semiconductor to be deposited on it nor can it be greatly etched by any of the chemicals involved in the deposition process. It should not reduce or oxidize during any procedure during or after growth.

(c)   The substrate must be thermally stable so that it does not crack, exfoliate, nor pass through a phase transition during any thermal treatment, especially during deposition of the semiconductor layer.

(d)   The thermal expansion coefficients of the substrate must match to within < 1 percent of the deposited layer. This is more critical for thick layers than for thin.

3.2.2 Substrate Criteria for GeO_2

A table of the physical properties of GeO_2 and elemental Ge is presented in Table I. Reference to this would suggest that the crystal structures are incompatible; however, if a surface in GeO_2 is selected which includes an oxygen packing layer such as {111}, this misfit difficulty may be over-come. GeO_2 is especially favorable in this respect since reduction in H_2 produces a thin layer of Ge metal on the exposed surface which could be a starting surface for further growth[1]. It would be necessary to in-vestigate the orientation between the Ge layer and the GeO_2 beneath, but {111} seems the most likely surface.

TABLE I
PHYSICAL PROPERTIES OF Ge AND GeO_2

Properties	Ge(18)	GeO_2(4)
Crystal Structure	diamond(cubic)	rutile(tet)
Space Group	Fd3m	P 4/mnm
Lattice Parameters Å	a = 5.657	a = 4.40 c = 2.87
Molecule/Cell	8	2
Atomic Weight	72.60	104.60
Density 25°C	5.32	6.277
Hardness (Vickers scale)	-	450 (20°C) 50 (600°C)
Melting Point	940°C	1086°C (transforms at 1000°C)
Boiling Point	2700°C	-
Band Gap	0.75 eV(0°K)	5.5
Intrinsic Resistivity, 27°C (ohm cm)	47	-
Electron Mobility, Drift, cm^2/Volt sec.	3800	-
Hole Mobility, Drift, cm^2/Volt sec.	1800	-
Debye Temperature	362°K	-
Thermal Conductivity (cal/sec cm°C)	0.15	-
Dielectric Constant	15.7	c 76.0 c 28.0
Specific Heat, 25°C (cal/gm°C)	0.074	-
Thermal Expansion Coefficient (linear) 25°C/(1°C)	6.1×10^{-6}*	12.7×10^{-6}†
Latent Heat of Fusion (cal/mol)	8300	-
Index of Refraction	> 4.0 (2.0µ to 16)	Visible NaD ω = 1.960 ϵ 2.047
Absorption edge, microns	1.6	0.2 (5.5 eV)

* 25°C cm^{-1}c^{o-1} only.
† 25°C - 1000°C cm^{-1} c^{o-1}

YHG R1

Thin films of silicon on quartz[19], space groups Fd3m and P3$_1$21 respectively, have been grown successfully and so has epitaxial growth of silicon on αAl_2O_3 (sapphire)[20]. In both cases the Si orientation followed that of the substrate. This would suggest that the degree of misfit for comparable substrate to deposited layer can be quite large in some instances.

Chemical Stability

GeO_2 seems to be chemically stable except in strongly reducing atmospheres where a layer of Ge metal is formed on the crystal surface; but as mentioned earlier, this may be an advantage. In view of this, it may be necessary to consider sputtering techniques for the final deposition of the Ge layer.

Thermal Expansion Coefficients

There is a question about the accuracy of the linear expansion coefficient of GeO_2. The best x-ray lattice parameter data available gives anomalous results in the 200-400°C range. Table II compares the lattice parameters and the calculated linear expansion coefficients α. When α is given by $\alpha = \dfrac{\Delta\ell}{\ell_0 \Delta t}$, ℓ = length, t = temp.

TABLE II
THERMAL EXPANSION OF Ge AND GeO$_2$

GE		GeO$_2$ (21)				
T	a_0 Å	T	a_0 Å	Δa_0	c_0 Å	Δc_0
20	5.648	24.25	4.404		2.870	
230	5.655	200.00	4.406	0.002	2.876	0.006
450	5.664	400.00	4.417		2.881	
600	5.681	600.00	4.424	0.007	2.888	0.007

Ge		GeO$_2$		
Temp. Range	α_{a_0} (x 10^{-4})	Temp. Range	α_a (x 10^{-6})	α_c (x 10^{-6})
20 - 230	5.90	26.25 - 200.00	2.61	12.03
230 - 450	7.23	200 - 400.00	7.84 extrapol. (12.48) calc.	12.03 extrapol. (8.69) calc.
450 - 600	7.69	400 - 600.00	7.92	12.14

From the data in Table II we can determine the linear expansion coefficient in the 200°C to 400°C range.

A plot of a_0 and c_0 vs temperature shows the anomaly at 200°C; the a_0 value is especially poor. Using the curve to find a_0 and c_0 at 200°C gives 4.410Å and 2.8755Å, respectively. Calculated α's from these values give α = 7.84 in the a direction and α = 11.02 in the c direction. However,

FIGURE 1: GeO_2 $A_0 - C_0$ Vs. Temperature C°.

II-15
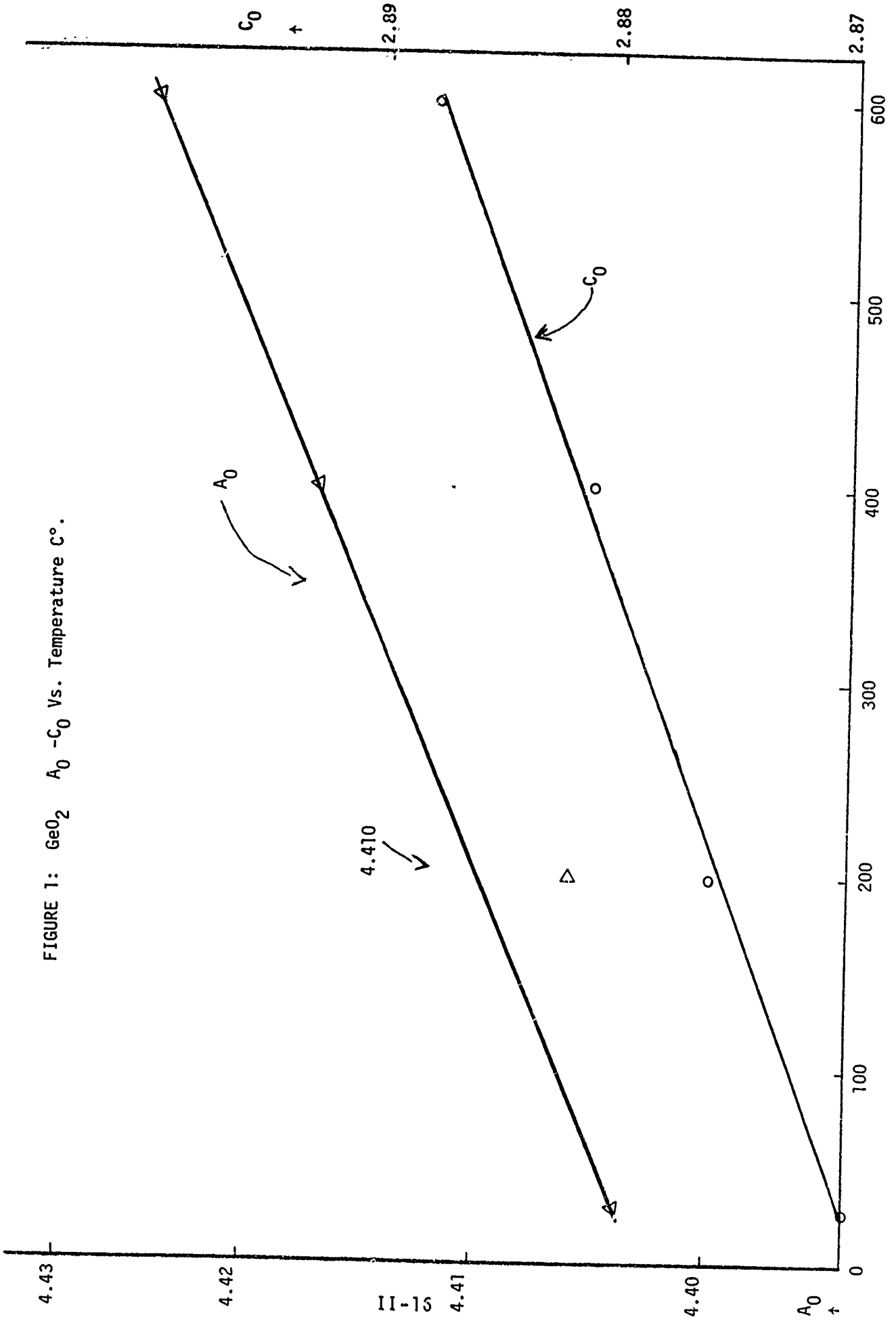
there is more scatter in the c_0 curve and an adjustment can be made so that c_0 extrapolated can equal 2.8750. This will give a calculated α of 12.03 x 10^{-6} cm^{-1} $C^{\circ-1}$, which is consistent with the other values in this direction.

In the {111} direction in GeO_2 the expansion coefficient would involve both α_a and α_c parameters. This indicates that if {111} were used as a substrate for Ge metal, the expansion coefficient over a temperature range 600 - 20°C should be closely matched.

3.3 Electrical Measurements

An obvious first electrical measurement to make in the Ge films might be of sheet resistivity using a common four point probe[22]. Interpretation of such a measurement, however, is likely to be difficult. For example, until it is known that the carrier mobility in the films is comparable with that of good quality bulk Ge, which would be the hoped for result but not the assured one, a high resistivity measurement could mean a low carrier concentration in good material, or simply a frankly lousy mobility. Similarly, a low resistivity could be due simply to degenerate doping and say nothing about film quality. A four point probe measurement is most useful once the magnitude of the mobility is known with confidence.

A better measurement would be a Hall effect or Van Der Pauw[23] measurement. Until it is shown that there is no anisotropy created in the films by the GeO_2 substrate, a Hall effect measurement would be preferred. To prepare a sample, a cross with two pairs of cross arms (the Cross of Lorraine[24]) should be masked out on the Ge surface. Black

Apiezon[25] wax dissolved in trichloroethylene and applied with a small paint-brush could be used for masking. The unwanted Ge could then be etched away using a Ge etch such as CP-4[26]. After the wax is dissolved off with trichloroethylene and the sample cleaned, contact can be made to the six arms and the measurements performed. This geometry has the advantages that two Hall measurements and two resistivity measurements can be made on the same sample for a consistency check, and that the current direction is determined. Once the uniformity and isotropy of the films is determined, a Van Der Pauw geometry[23] could be used with confidence.

The room temperature electron and hole mobilities in high quality Ge[27] range from 5,000 cm^2/V-sec and 2,000 cm^2/V-sec, respectively, at a carrier concentration of 10^{14} cm^2/V-sec, to 1,000 cm^2/V-sec and 100 cm^2/V-sec at a concentration of 10^{19} cm^3. The mobilities in the films are expected to be somewhat lower; how much lower they are is a good indication of the purity and perfection of the films. If initial measurements are promising the next step is to vary the temperature. Lattice scattering becomes less important at reduced temperatures and thus impurities and imperfections are even more evident. Measurements made to liquid nitrogen temperature, 77°K, for example, would also yield valuable information on the concentration and nature of donors and acceptors. It will also be necessary to intentionally dope the Ge films. This can be done by diffusion after the films are produced or during growth, if the films are deposited. For diffusion, diffusion source solutions are available from the Emulsitone Company[28], which might be useful in a laboratory not otherwise equipped to do semiconductor diffusions.

Ultimately, one can envision applying the full force of the silicon-germanium device technologies to Ge formed by reduction on GeO_2 but only if this Ge can be shown to be of good quality. Such envisioning is thus premature at this time; the straightforward mobility and carrier concentration measurements outlined and the correction of these results with film doping purity and crystallinity information is the first order of business.

4.0 GeO_2 AS A POLARIZER

4.1 Background

Polarizer development for lasers has taken three principle directions.
These are:

1) Improvement of efficiency (i.e., improved "energy" efficiency
for a given polarization efficiency)

2) Development of polarizer materials for the new laser wavelengths, and

3) Development of polarizer for high-power laser systems.

Energy efficiency in polarization can be improved in many instances
by using birefringent crystals. In modern crystal polarizers, the beam is
split into two mutually orthogonal polarization forms, each polarization
form being 100% polarized. Each class of crystal polarizers is made up of
two identical crystal segments and is distinct in the manner in which these
segments are joined. Each polarizer class is distinct in the method in
which the two polarization forms of the beams are spatially separated.
Within a given class, however, polarizers will vary only in their usable
wavelength range, losses, maximum power level usable and the magnitude of
the separation of the two polarized components. These last factors depend
upon the nature of the material, especially its optical transmission, its
radiation damage threshold and the magnitude of its birefringence (i.e.,
its difference in refractive indices along different crystal directions).
The class of birefringent polarizers is illustrated in the following table:

TABLE III

TYPES OF POLARIZERS

Polarizer Class		Comments
Glan-Thompson	Cement $n \leq n_e$ $n_0 = 1.66$ $n_e = 1.49$ O.A.	Not generally suitable for high-power laser applications due to deterioration of required joining cement.
Glan-Foucault	O.A. $n_0 = 1.66$ $n_e = 1.49$ O.A.	Angle chosen for total internal reflection of polarization component. Acceptance angle small, e.g. 7° for Calcite. However, this is not bad for lasers. Stray reflection problems from side surfaces.
Rochon	O.A. O.A.	One beam is axial. Acceptance angle intermediate between Glan-Foucault and Wollaston
Wollaston	O.A. O.A.	Both beams diverted. Highest acceptance angle for a given material.
Nicol	O.A. 68°	Very difficult because of obliquity of both faces to optic axis. Requires cement. Causes astigmatism due to obliquity of entrance/exit faces.

II-21

YHG R1

The specific use of GeO_2 as a laser polarizer seems to be restricted to the Glan-Foucault, Rochon or Wollaston forms. The first consideration as to class or type appears to be the requirement (or lack thereof) of an "undiverted beam". It is probable that obtaining a 100% polarized un-diverted, or coaxial, beam is desirable, therefore it appears that GeO_2 should be considered for polarizer designs of either (or both) the Glan-Foucault or Rochon type. For the G-T polarizer, one beam is internally re-flected, while in the Rochon polarizer both beams are transmitted but are separated by an angular divergence, which depends upon the magnitude of the birefringence.

Present polarizers of the G-T, Rochon and Wollaston types generally em-ploy calcite ($CaCO_3$) (out to ~ 3 microns) and quartz (out to ~ 3μ), with the Rochon type being more applicable, for a given material, to higher power density usage, e.g. to 100 megawatts (pulsed) for calcite-quartz combin-ations. The following discussion applies to Rochon type polarizers because of their applicability in lasers.

4.2 Characteristics of GeO_2 Rochon Polarizers

Tetragonal GeO_2 is a uniaxially/positive birefringent crystal. For the sodium lines, the ordinary and extraordinary refractive indices are n_o = 1.960 and n_e = 2.047 respectively, with Δn = 0.087.

Since the propagation direction of both polarization components in the first crystal is parallel to the optic axis, both components are character-ized by the ordinary index, n_o. In the second crystal, the propagation of one of the components (the extraordinary one) becomes governed by the

extraordinary index, n_e, since propagation is now perpendicular to the optic axis. This component undergoes refraction, governed by the equation

$$n_0 \sin \Theta_{11} = n_e \sin \Theta_{+1} \tag{1}$$

By geometry, the angle of incidence onto interface between the two crystals is just the prism angle α, so that the angle of refraction at this surface is just

$$\Theta_{+1} = \sin^{-1} \left(\frac{n_0 \sin \alpha}{n_e} \right) \tag{2}$$

At the last surface of the second crystal the angle of incidence, Θ_{12}, is given by

$$\Theta_{12} = (\alpha - \Theta_{r1}) \tag{3}$$

Assuming the external medium to be air, then the angle of refraction is

$$\Theta_{r2} = \sin^{-1} (n_0 \sin \Theta_{12}) \tag{4}$$

or in terms of the parameters n_0, n_e and α

$$\Theta_{r2} = \sin^{-1} [\sin \alpha (n_e^2 - n_0^2 \sin^2 \alpha)^{1/2} - n_0 \sin \alpha \cos \alpha] \equiv \Theta_d \tag{5}$$

This angle, $\Theta_{r2} \equiv \Theta_d$, represents the angular divergence of the emergent polarization components.

For emergent beam divergence characteristics, one may choose α to optimize the angular separation of the ordinary and extraordinary components. The optimum prism angle is a function only of the indices n_0 and n_e and is given by the solution of the equation

$$x = 1/2 \, (n_e/n_0)^2 + (1-2x) \left[\frac{(1-x) + \Delta n/n_0 \, (2 + \Delta n/n_0)}{(1-x)} \right]^{1/2} \quad (6)$$

where $x \equiv \sin^2 \alpha$. As a first approximation, assuming small Δn, the optimum angle is

$$\alpha = \sin^{-1} \left[\frac{1}{2} (1 + n_e^2 / n_0^2)^{1/2} \right] \quad (7)$$

Evaluating Equation (7), we find the optimum value for $\alpha = 46.9°$. Using this value in Equation (5), the deflection angle of the extraordinary ray is $5.28°$, a small but usable amount for laser applications. The deflection for other values of α are shown in Table III.

α Degrees	Θ_d Degrees
30	3.32
45	4.76
46.9	5.28
60	internally reflecting

This analysis assumes normal incidence of the entering ray. If incidence other than normal occurs, a question of the purity of the polarized beams arises. We expect to consider this condition and report on it subsequently.

5.0 CONCLUSIONS

The tetragonal form of GeO_2 has several potential applications as discussed in this report. All of them need to have further detailed examination for successful use. Consideration should be given to the several applications, and the greatest effort directed at the most significant area, while allowing for the estimated difficulty.

REFERENCES

1. J. W. Goodrum, Top-seeded Flux Growth of Tetragonal GeO_2, J. Crystal Growth, $\underline{7}$, p. 254-256 (1970).

2. C. E. Ryan, Mat. Res. Bull. $\underline{4}$ (1969) S-1.

3. C. G. Fonstad and R. H. Rediker, J.A.P., to be published; R. H. Rediker, OAR Res. Rev. $\underline{4}$ (1970) 16.

4. IV-VI Semiconducting Compounds Data Tables compiled by M. Neuberger (Electronics Properties Information Center, Hughes Aircraft Co., Culver City, Calif., 1969), p. 5.

5. S. Zwerdling and S. Sheff, J. Electrochem. Soc. $\underline{107}$ (1960) 338.

6. R. D. Wales, J. Electrochem. Soc. $\underline{111}$ (1964) 478.

7. H. A. Papazian, J. Appl. Phys. $\underline{27}$ (1956) 1253.

8. Handbook of Chemistry and Physics, 43rd Edition (Chemical Rubber Co., 1961) p. 2560.

9. H. J. van Daal, J. Appl. Phys. $\underline{39}$ (1968) 4467.

10. F. J. Arlinghaus and W. A. Albers, Jr., Proc. of Density of States Conf., N.B.S., Gaithersberg, Md.,Nov. 1969.

11. J. Bardeen and W. Shockley, Phys. Rev. $\underline{80}$ (1950) 72.

12. M. F. C. Ladd, Acta Cryst. $\underline{A25}$ (1969) 486.

13. A. J. Dekker, Solid State Physics, Prentice Hall, Inc., Englewood Cliffs, N.J., p. 149 (1965).

14. R. A. Griener, Semiconductor Devices and Applications (McGraw-Hill Book Co., Inc., New York, 1961) p. 77.

15. Ibid., p. 81.

16. J. H. Becker and W. R. Hosler, Phys. Rev. $\underline{137}$ (1965) A1872.

17. C. A. Mead, S. S. Electr. $\underline{9}$ (1966) 1023.

REFERENCES (Cont'd)

18. Dunlap, C. W., <u>An Introduction to Semiconductors</u>, J. Wiley & Son
    p. 225 (1957).

19. Bicknell, R. W., <u>et al</u>, The Epitaxial Deposition of Silicon on
    Quartz, Phil. Mag., <u>7</u>, p. 965-979 (1962).

20. Manasevit, H., and Simpson, W.I., Single Crystal Silicon on a
    Sapphire Substrate, J. Appl. Phys. <u>35</u>, p. 1349-1351 (1964).

21. Majundar, A. J., and Roy, R., J. Inorganic Nuclear Chem. <u>27</u>,
    p. 1961-1973 (1965).

22. R. A. Griener, Ibid., p. 78

23. L. J. Van der Pauw, Philips Res. Rpts. <u>13</u> (1958) 1.

24. <u>Websters Seventh New Collegiate Dictionary</u> (G. and C. Merriam Co.,
    Springfield, Mass., 1963) p. 198.

25. Apiezon Products, Ltd.

26. <u>Transistor Technology</u>, Vol. I., Ed. by Bridges, Scaff, and Shive, p. 354.

27. S. M. Sze, <u>Physics of Semiconductors</u>, (John Wiley, New York,
    1969), p. 40.

28. Emulsitone Company, P.O. Box 39, Livingstone, N.J. 07039.

Part III

MEDIUM GAIN, HIGH ENERGY STORAGE NEODYMIUM LASER MATERIALS

1.0 INTRODUCTION

The development of more sophisticated military systems employing lasers requires a parallel development of laser materials which have the necessary performance characteristics for a particular application. (See Figure 1.) Two examples of such specialized laser devices are the Nd:YAG and Nd:glass lasers. As materials, Nd:YAG is ideally suited for high average power, high frequency applications while Nd:glass lies in the realm of low frequency, very high peak powers. Presently, ruby provides a laser source with characteristics in the region between YAG and glass lasers. Ruby, however, does not provide a covert source for the military systems.

The basic requirements for such a laser material in this intermediate region are 1) that it have a lower gain than Nd:YAG in order to increase the energy storage capabilities; and 2) that it have better thermal properties than Nd:glass so that high average power can be generated on a continuous, rather than intermittent, basis. Operation at 1.06μ would make it compatible with many existing systems, an obvious advantage.

A unique material with these very properties has been grown at AFCRL. This crystal, Nd:Sodium Germanate, displays a very broad fluorescence, similar to Nd:glass, and a short lifetime. Its thermal properties are estimated to be similar to ruby. This material serves as an ideal host for the neodymium ion and will, consequently, fill the high average power, high peak power gap between glass and YAG.
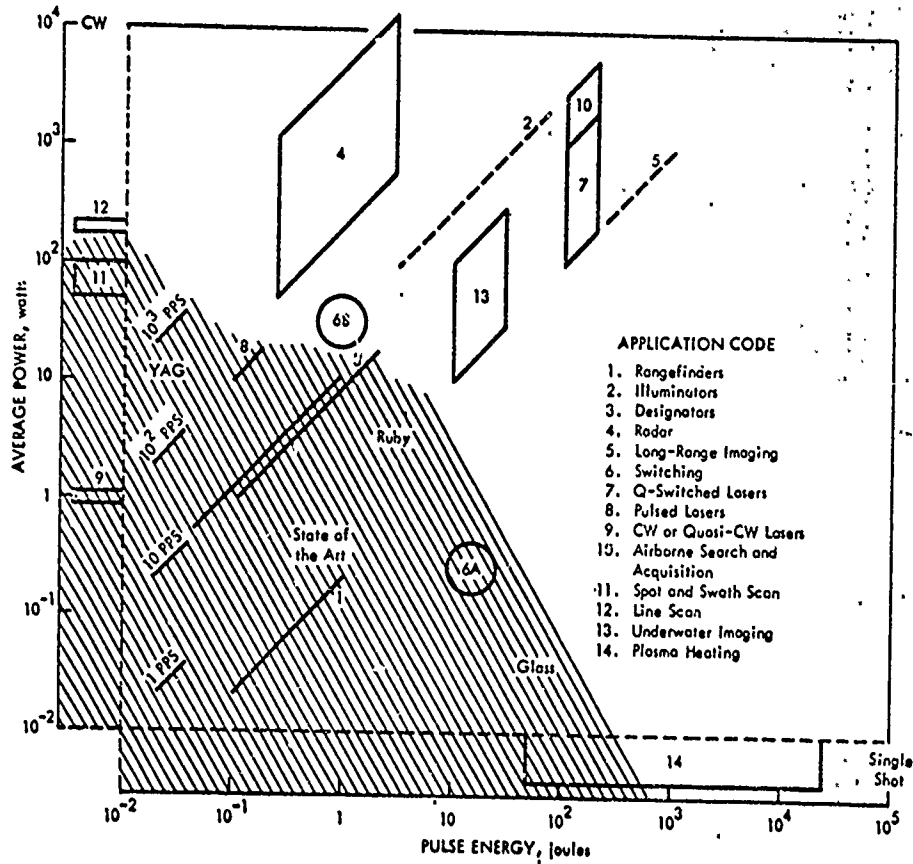
FIGURE 1. Power and Energy Requirements for Laser Applications

This report is an analysis of the thermal and spectro-
scopic properties of laser materials. The intent is to
provide a means for quickly determining those system applica-
tions which most effectively utilize the specific properties
of a new material, or to provide a guide when seeking for a
new material to fill a particular application. In particular,
this report examines the properties of sodium germanate as a
host crystal for the Nd laser ion.

This report is divided into five sections. The second
section deals with physical effects which limit the laser
output. The interrelation between (a) the material constants,
(b) the maximum average pump power, and (c) single high energy
pump pulse, allows the maximum laser output before fracture
to be determined. Furthermore, the effect of pre-lasing on
laser output is also evaluated, as it limits the output of
pulsed laser systems. The third section is a brief dis-
cussion of pump lamps and their relevant parameters for this
analysis. Section 4 is an analysis of repetitively Q switched
and pulsed laser systems. The essential relationships be-
tween the spectroscopic and physical properties of the materials
and the laser output have been included. Section 5 is a
comparison of the laser materials. The laser system proper-
ties of the materials are evaluated based on the results of
Sections 2, 3 and 4 and tabulated.

This analysis yields the important result that the
germanates, in particular, the sodium germanate crystal,
possess unique properties which enable them to provide a
covert source with unexcelled output characteristics. Based
on estimates of the thermal properties of the germanates,
their fracture limits are about half that of YAG for average

III-3

power and 3-4 times that of YAG for single pulse operation.
Whereas the germanates could be operated on a CW basis from
thermal considerations, their thresholds are very high and
would be difficult to achieve with currently available pump
lamps. In short, the germanates can satisfy the need for a
covert pulsed source with both high average and high peak power.

The chart below reveals, at a glance, the relative capa-
bilities of the materials investigated. This chart though not
very quantitative, clearly places the germanates right behind
ruby as a high peak high average power laser host. In this
chart, "1" corresponds to the material with the most desirable
properties on a 1-5 scale. The totals at the bottom indicate
the relation of one material to another on a 3 to 15 scale. A
quantitative comparison is presented in Table VIII.

	YAG	Glass	Ruby	YLF	Germanates
High Average Power	5	4	1	3	2
High Peak Power (One Pulse)	5	1	2	4	3
High Peak Power (50pps)	5	4	1	3	2
	15	9	4	10	7

2.0 LIMITING PHYSICAL PROPERTIES

The dependence of thermal fracture, energy storage and pre-lasing on the material parameters is obtained in this section. In later sections the laser output will be determined in terms of the maximum heat which the rod can absorb before fracture, or in terms of the maximum heat which can be absorbed before pre-lasing occurs, whichever is smaller.

2.1 THERMAL FRACTURE

Thermal Fracture - High Average Pump Power

Thermal stresses from pumping at high repetition rates or CW will fracture a laser rod if they exceed the tensile strength of the material. An analysis by Koechner [1] shows that for a cylindrical rod with uniform heat absorption throughout its volume the temperature, $T(r)$, inside the rod is given by

$$T(r) = \frac{U_{heat}}{2k} (r_o^2 - r^2) \tag{1}$$

and the tangential stress, σ_θ, is given by

$$\sigma_\theta = \left(\frac{U_{heat} V \alpha_T E}{16(1-\nu)k\pi \ell_{rod}} \right) \left(-1 + 3 \frac{r^2}{r_o^2} \right) \tag{2}$$

where

U_{heat} is the rate of heat generation per unit volume in the laser rod

V is the volume of the laser rod

α_T is the thermal expansion coefficient

E is Young's modulus

ν is Poisson's ratio

k is the thermal conductivity

ℓ_{rod} is the length of the rod

r_o is the radius of the rod.

The tangential stress, σ_θ, is always larger than the radial stress, σ_r, and equal in magnitude to the largest axial stress, σ_z (at $r = 0$ or $r = r_o$).

The total heat flow out of the rod, $U_{heat}V$, depends on the type of pump lamp used. U_{heat} will, therefore, have to be evaluated for each pump-lamp/rod combination. The best lamp/rod match would most likely be determined by the efficiency with which the lamp pumps the upper laser level. The maximum value of U_{heat} before fracture, which will be called $U_{max, fracture}$ can be determined from equation (2) once σ_θ is known. If A is the cross sectional area of the rod then

$$U_{max, \text{ fracture}} = \frac{8\pi k(1 - \nu)\sigma_\theta}{\alpha_T EA} . \tag{3}$$

Given the material constants k, ν, σ_θ, α_T and E, estimates of $U_{max, \text{ fracture}}$ can be computed for the various laser materials. These values are shown in row 1 of Table VII. It will be assumed that $A = (\pi/10)cm^2$, corresponding to a rod 1/4" in diameter.

Thermal Fracture - Single Pump Pulse

A different model has to be used to analyze thermal fracture from a single, high energy, flashlamp pulse. This model assumes that fracture occurs when the temperature gradient at the surface exceeds a critical value which depends on the total amount of energy absorbed during the flashlamp pulse. It also assumes that the temperature at every point in the crystal rises uniformly and instantaneously with no heat conduction occurring until after the pump pulse is gone. Since the pump pulse is considered an impulse function at t_o, temperature gradients will be set up in the laser rod for $t > t_o$.

The heat conduction equation for an isotropic, cylindrical rod is:

$$\frac{\partial^2 T}{\partial r^2} = \frac{\rho C}{k} \frac{\partial T}{\partial t} \quad (t > t_o). \tag{4}$$

The solution to this equation is

$$T = T_o \, e^{-t/\tau} \cos \Lambda r \quad (t > t_o).$$ (5)

Inserting this equation into equation (4) yields a condition on Λ: $\quad \Lambda^2 = \dfrac{\rho C}{k\tau}$.

The boundary conditions:

$$\frac{\partial T}{\partial r} = 0 \quad \text{at } r = 0,$$

and (6)

$$T = 0 \quad \text{at } r = r_o,$$

allow Λ and τ to be determined:

$$\Lambda = \frac{\pi}{2 r_o} = \sqrt{\frac{\rho C}{k\tau}} \; ;$$ (7)

Also, since $\Lambda^2 = \dfrac{\rho C}{k\tau}$ we find that

$$\tau = \frac{4 \rho C r_o^2}{\pi^2 k} .$$ (8)

This result is identical with that of equation (9) of reference (26) except that the constant in the denominator is 4.3 instead of $\dfrac{\pi^2}{4} = 2.46$. This difference can be attributed to the fact that (26) incorporated many terms of the series solution to equation (4), whereas, we have only taken the first term.

The temperature T_o at the center of the rod at $t = t_o^+$ can be evaluated by relating the total heat energy absorbed by the laser rod, H_{heat}, to the temperature rise in the material through

$$dH_{heat} = \rho C T dV$$

$$\int_o^{r_o} dH_{heat} = \rho C T_o e^{-t/\tau} \int_o^{r_o} \cos(\Lambda r)(2\pi r \ell_{rod})dr$$

$$H_{heat} = (2\pi \ell_{rod} \rho C T_o e^{-t/\tau})(\frac{\pi}{2} - 1)\left(\frac{2 r_o}{\pi}\right)^2 \qquad (9)$$

$$T_o = \left(\frac{\pi H_{heat}}{8\ell_{rod}\rho C \left(\frac{\pi}{2} - 1\right) r_o^2}\right) . \qquad (10)$$

Since H_{heat} is known, T_o can be computed.

The maximum energy absorbed before fracture, which will be called $H_{max, fracture}$, can now be determined from equation (1) for a uniform rate of heat absorption and from $T(r)$ from equation (5). The maximum temperature gradient occurs at r_o, and is obtained by differentiating equation (1):

$$\frac{dT}{dr} = -\frac{U_{heat}\, r_o}{k} \tag{11}$$

The maximum tolerable gradient occurs for $U_{heat} = U_{max,fracture}$. Thus

$$\left.\frac{dT}{dr}\right|_{max} = -\frac{U_{max,\,fracture}\, r_o}{k} \; . \tag{12}$$

From equation (5), we have

$$\frac{dT}{dr} = -\frac{\pi T_o}{2r_o} \tag{13}$$

at $t = t_o^+$, $r = r_o$. Equating the gradients obtained from equations (12) and (13), we find,

$$\frac{\pi T_o}{2r_o} = \left(\frac{U_{max,\,fracture}}{k}\right) r_o \; . \tag{14}$$

Therefore,

$$\frac{\pi^2 H_{max,fracture}}{16\ell_{rod}\, \rho C(\frac{\pi}{2} - 1)r_o^{\,3}} = \left(\frac{U_{max,\,fracture}}{k}\right) r_o \tag{15}$$

$$H_{max,\,fracture} = \left(\frac{16\ell_{rod}(\frac{\pi}{2} - 1)r_o^{\,4}}{\pi^2}\right)\left(\frac{\rho C}{k}\right) U_{max,fracture}$$

$$H_{max,\,fracture} = \left(\frac{16\ell_{rod}(\frac{\pi}{2} - 1)r_o^{\,4}}{\pi^2}\right)\left(\frac{\rho C}{k}\right) U_{max,\,fracture} \tag{16}$$

$$H_{max,fracture} = (0.092)\left(\frac{\rho C}{k}\right) U_{max,\,fracture} \; .$$

is the maximum heat energy the laser rod can absorb before fracture (see row 3 of Table VII for a comparison of various laser materials). An important relationship between the material parameters can be obtained by inserting equation (3) for $\dot{U}_{max, \text{ fracture}}$ into the above equation.

$$H_{max \text{ fracture}} = \left(\frac{128\left(\frac{\pi}{2} - 1\right) V}{\pi^3}\right)\left(\frac{\rho C}{\alpha_T}\right)\left(\frac{(1 - \nu)\sigma_\theta}{E}\right) . \quad (17)$$

where

$$128\left(\frac{\pi}{2} - 1\right)V/\pi^3 = 7.4 \text{cm}^3.$$

The thermal properties are all contained in the term

$$(\rho C)\left(\frac{(1 - \nu)\sigma_\theta}{\alpha_T E}\right) .$$

YHG R1

The first term, (ρC), is proportional to how much heat one can store in the material (per unit volume) and the second term $\left[\dfrac{(1 - \nu)\sigma_\theta}{\alpha_T E}\right]$ tells how fragile the material is.

2.2 LASER ENERGY OUTPUT

The energy output per pulse is also a parameter which is included in the figure of merit of a laser material. The energy output per pulse depends directly on the amount of energy which can be stored in the laser rod prior to emission of the laser pulse and pre-lasing which depletes the upper level population prematurely. Expressions for energy storage and pre-lasing are derived below.

Energy Storage

Quite simply, the energy output can be written as

$$E_{laser} = \eta h \nu \Delta N V \qquad (18)$$

where $(h\nu)$ is the energy of each lasing photon,

$$\eta = \frac{\tau_u \text{ (measured lifetime)}}{\tau_{sp} \text{ (spontaneous lifetime)}}$$

is the fraction of atoms in the upper laser level which become laser photons[*] (2), and ΔN is the population inversion per unit volume of the two laser levels. The population inversion is given by

$$\Delta N = \frac{\left(f_{fluor}\right)Q\left(\frac{\tau_u}{\tau_{1amp}}\right)\left(P_p - P_{th}\right)}{\eta h\nu V} , \qquad (19)$$

where

f_{fluor} is the fraction of pump power absorbed in the pump bands which could make the laser transition,

Q is the fluorescent efficiency from the pump bands to the upper laser level,

P_p is the pump power

P_{th} is the threshold pump power

---

[*]Note that $\left(\frac{\tau_u}{\tau_{sp}}\right)$ is just the quantum efficiency of the level of reference (3) equation (10).

YHG R1

E_{laser}, therefore, is given by

$$E_{laser} \approx f_{fluor} \, \eta Q P_p \tau_u \gamma \qquad (20)$$

since ($f_{fluor} \, \eta Q$) is just the fraction of absorbed pump energy which makes the laser transition,

and

$$\gamma = \begin{cases} 1 & \text{if } \tau_u \geq \tau_{lamp} \\[2ex] \dfrac{\tau_u}{\tau_{lamp}} & \text{if } \tau_u < \tau_{lamp} \end{cases} \qquad (21)$$

where τ_{lamp} is the duration of the pump pulse. It has also been assumed that $P_p \gg P_{th}$.

The parameter γ is the fraction of pump pulse energy which can be stored in the upper laser level. Since the population of the upper laser level will decay after a time, τ_u, only the fraction γ of a pump pulse longer than τ_u will be utilized.

Let us also define f_o as the ratio of the amount of heat generated per unit volume to the amount of 1.06μ fluorescence generated per unit volume, i.e.,

$$\frac{U_{heat}}{U_{fluor}} = \frac{H_{heat}}{H_{fluor}} = f_o = \frac{f' - f_{fluor} \eta Q}{f_{fluor} \eta Q} \tag{23}$$

where f' is the fraction of total pump lamp energy absorbed.

Therefore,

$$f_{fluor} \eta Q P_p \tau_u \approx \frac{H_{fluor}}{\gamma} = \frac{H_{heat}}{f_o} \tag{24}$$

and so

$$E_{laser} = \frac{H_{heat} \gamma}{f_o} . \tag{25}$$

Using equation (17) for H_{heat}, E_{laser} becomes

$$E_{laser} = \left(\frac{16 \ell_{rod} \left(\frac{\pi}{2} - 1 \right) r_o^4}{\pi^2} \right) \left(\frac{\rho C}{k} \right) \left(\frac{\gamma U_{heat}}{f_o} \right) \tag{26}$$

Replacing U_{heat} by its maximum value $U_{max, fracture}$, we obtain the largest energy output before fracture $E_{laser max, fracture}$ (row 6, Table VII).

III-15

Pre-Lasing

Another effect which limits the amount of energy a laser material can store is pre-lasing. Pre-lasing occurs when the gain in the laser medium is high enough to cause oscillations even off low reflection surfaces.

The population inversion (energy stored) at threshold is obtained by setting the gain equal to the losses

$$g_o \ell = L + T,$$

where, equations (6) and (7) of reference (4) give

$$g_o = \frac{\lambda^2 \Delta N}{8 \pi n^2 \Delta \nu \tau_{sp}} = \sigma \Delta N \qquad (29)$$

for a four level laser where ΔN is given by equation (19) and σ is the stimulated emission cross section at the laser line peak. The laser energy (equation (18)) is, then simply

$$E_{\substack{laser \\ pre-lase}} = \eta h \nu V \Delta N \left(\frac{L + 1}{\ell \sigma_{rod}} \right) (\eta h \nu V)$$

$$E_{\substack{laser \\ pre-lase}} = \left[\frac{(L + 1)(\eta h \nu V)}{\ell_{rod}} \right] \left(\frac{1}{\sigma} \right)$$

Here we have set $T = 1$ corresponding to antireflection coatings. $E_{laser\ pre-lase}$ is computed and given in row (9) of Table VII.

It should be pointed out that it is the cross section, σ, which determines the stored energy for pre-lasing. Materials with lower values of σ will be able to store larger amounts of energy, because they have a higher threshold for pre-lasing.

3.0 PUMP LAMPS

The choice of pump lamp is extremely important not only to lower the threshold but also to minimize unwanted heat generation. Ideally, one should pump only in the pump band nearest the upper laser level. Unfortunately, such lamps are not available.

The pump bands of Nd in various hosts have different breadths, absorption strengths, and quantum efficiencies. These pump bands can be matched to various pump lamps to obtain the conversion efficiency of lamp power to upper laser level fluorescent power and to heat.

A comparison of several lamps which are available is made in this section. Tables I, II, III and IV are adapted from those in (5). Table V compares the ability of the lamps to pump the different laser materials indicated. For comparison, ruby is included.

Table 1a - Xenon Pumped Nd:YAG Laser Analysis

Absorption Band	Relative Strength	Amount to Fluorescence	Amount to Heat	5750 A/cm²			16700 A/cm²		
				Lamp Power in Band	Lamp Power to Fluorescent Power	Lamp Power to Heat	Lamp Power in Band	Lamp Power to Fluorescent Power	Lamp Power to Heat
0.51 to 0.54	1/3	0.49	0.51	30	15	15	85	42	43
0.57 to 0.59	1/2	0.55	0.45	37	21	17	112	62	50
0.73 to 0.76	1	0.70	0.30	60	42	18	135	95	40
0.79 to 0.82	1	0.76	0.24	45	34	11	150	114	36
0.87 to 0.89	1/5	0.83	0.17	12	10	2	33	27	6

Table 1b - Krypton Pumped Nd:YAG Laser Analysis

Absorption Band	Relative Strength	Amount to Fluorescence	Amount to Heat	5400 W/cm²			15000 W/cm²		
				Lamp Power in Band	Lamp Power to Fluorescent Power	Lamp Power to Heat	Lamp Power in Band	Lamp Power to Fluorescent Power	Lamp Power to Heat
0.51 to 0.54	1/3	0.49	0.51	25	12	13	75	37	38
0.57 to 0.59	1/2	0.55	0.45	33	18	15	105	58	47
0.73 to 0.76	1	0.70	0.30	60	42	18	105	74	31
0.79 to 0.82	1	0.76	0.24	75	57	18	210	160	50
0.87 to 0.89	1	0.83	0.17	12	10	2	24	20	4

Table Ic - Tungsten Pumped Nd:YAG Laser Analysis

Absorption Band	Relative Strength	Amount to Fluorescence	Amount to Heat	228 W/cm^2			
				Lamp Power in Band	Lamp Power to Fluorescent Power	Lamp Power to Heat	
0.51 to 0.54	1/3	0.49	0.51	0.9	0.45	0.45	
0.57 to 0.59	1/2	0.55	0.45	1.8	0.99	0.81	
0.73 to 0.76	1	0.70	0.30	4.5	3.1	1.4	
0.79 to 0.82	1	0.76	0.24	5.4	4.1	1.3	
0.87 to 0.89	1/5	0.83	0.17	0.9	0.75	0.15	

Table Id - Potassium Mercury Pumped Nd:YAG Laser Analysis

Absorption Band	Relative Strength	Amount to Fluorescence	Amount to Heat	100 W/cm^2		
				Lamp Power in Band	Lamp Power to Fluorescent Power	Lamp Power to Heat
0.51 to 0.54	1/3	0.49	0.51	0.4	0.2	0.2
0.57 to 0.59	1/2	0.55	0.45	0.9	0.5	0.4
0.73 to 0.76	1	0.70	0.30	4.2	2.9	1.3
0.79 to 0.82	1	0.76	0.24	6.3	4.8	1.5
0.87 to 0.89	1/5	0.83	0.17	0.3	0.25	0.05

Table IIa - Xenon Pumped Nd:Glass Laser Analysis

Absorption Band	Relative Strength	Amount to Fluorescence	Amount to Heat	5750 A/cm²			16700 A/cm²		
				Lamp Power in Band	Lamp Power to Fluorescent Power	Lamp Power to Heat	Lamp Power in Band	Lamp Power to Fluorescent Power	Lamp Power to Heat
0.51 to 0.54	1/2	0.5	0.5	30	15	15	87	44	43
0.57 to 0.59	1	0.55	0.45	50	23	27	150	83	67
0.73 to 0.76	1	0.69	0.31	40	28	12	90	62	28
0.79 to 0.82	1	0.75	0.25	30	23	7	100	75	25
0.87 to 0.89	1/2	0.83	0.17	35	29	6	65	54	11

Table IIb - Krypton Pumped Nd:Glass Laser Analysis

Absorption Band	Relative Strength	Amount to Fluorescence	Amount to Heat	5450 A/cm²			13000 A/cm²		
				Lamp Power in Band	Lamp Power to Fluorescent Power	Lamp Power to Heat	Lamp Power in Band	Lamp Power to Fluorescent Power	Lamp Power to Heat
0.51 to 0.54	1/2	0.5	0.5	25	12	13	75	38	37
0.57 to 0.59	1	0.55	0.45	40	22	18	130	71	59
0.73 to 0.76	1	0.60	0.31	30	21	9	70	48	27
0.79 to 0.82	1	0.75	0.25	50	38	12	140	105	35
0.87 to 0.89	1/2	0.83	0.17	25	21	4	45	37	8

YHG R1

Table IIc - Tungsten Pumped Nd:Glass Laser Analysis

Absorption Band	Relative Strength	Amount to Fluorescence	Amount to Heat	228 W/cm^2		
				Lamp Power in Band	Lamp Power to Fluorescent Power	Lamp Power to Heat
0.51 to 0.54	1/2	0.5	0.5	0.09	0.45	0.45
0.57 to 0.59	1	0.55	0.45	2.4	1.3	1.1
0.73 to 0.76	1	0.69	0.31	3.0	2.1	0.9
0.79 to 0.82	1	0.75	0.25	3.6	2.7	0.9
0.87 to 0.89	1/2	0.83	0.17	1.6	1.3	0.3

Table IId - Potassium Mercury Pumped Nd:Glass Laser Analysis

Absorption Band	Relative Strength	Amount to Fluorescence	Amount to Heat	100 W/cm^2		
				Lamp Power in Band	Lamp Power to Fluorescent Power	Lamp Power to Heat
0.51 to 0.54	1/2	0.5	0.5	0.3	0.15	0.15
0.57 to 0.59	1	0.55	0.45	1.0	0.55	0.45
0.73 to 0.76	1	0.69	0.31	3.8	2.6	1.2
0.79 to 0.82	1	0.75	0.25	4.6	3.4	1.2
0.87 to 0.89	1/2	0.83	0.17	0.7	0.6	0.1

YHG R1

Table IIIa - Xenon Pumped Nd:YLF Laser Analysis

Absorption Band	Relative Strength	Amount to Fluorescence	Amount to Heat	5750 A/cm²			16700 A/cm²		
				Lamp Power in Band	Lamp Power to Fluorescent Power	Lamp Power to Heat	Lamp Power in Band	Lamp Power to Fluorescent Power	Lamp Power to Heat
0.51 to 0.54	0.1	0.49	0.51	30	15	15	85	42	43
0.57 to 0.59	.5	0.55	0.45	125	69	56	375	210	165
0.73 to 0.76	1.0	0.70	0.30	200	140	60	450	315	135
0.79 to 0.82	1.0	0.75	0.25	150	113	37	500	375	125
0.87 to 0.89	0.5	0.84	0.16	175	147	28	325	270	55

Table IIIb - Krypton Pumped Nd:YLF Laser Analysis

Absorption Band	Relative Strength	Amount to Fluorescence	Amount to Heat	5400 A/cm²			15000 A/cm²		
				Lamp Power in Band	Lamp Power to Fluorescent Power	Lamp Power to Heat	Lamp Power in Band	Lamp Power to Fluorescent Power	Lamp Power to Heat
0.51 to 0.54	0.1	0.49	0.51	25	13	12	75	37	38
0.57 to 0.59	0.5	0.55	0.45	110	61	49	350	193	157
0.73 to 0.76	1.0	0.70	0.30	175	122	53	350	245	105
0.79 to 0.82	1.0	0.75	0.25	250	187	63	700	525	175
0.87 to 0.89	0.5	0.84	0.16	125	105	20	225	189	36

YHG R1

Table IIIc - Tungsten Pumped Nd:YLF Laser Analysis

Absorption Band	Relative Strength	Amount to Fluorescence	Amount to Heat	Lamp Power in Band	228 W/cm^2	
					Lamp Power to Fluorescent Power	Lamp Power to Heat
0.51 to 0.54	0.1	0.49	0.51	0.9	0.45	0.45
0.57 to 0.59	0.5	0.55	0.45	6.0	3.3	2.7
0.73 to 0.76	1.0	0.70	0.30	15	10.5	4.5
0.79 to 0.82	1.0	0.75	0.25	18	13.5	4.5
0.87 to 0.89	0.5	0.84	0.16	8	6.7	1.3

Table IIId - Potassium Mercury Pumped Nd:YLF Laser Analysis

Absorption Band	Relative Strength	Amount to Fluorescence	Amount to Heat	Lamp Power in Band	100 W/cm^2	
					Lamp Power to Fluorescent Power	Lamp Power to Heat
0.51 to 0.54	0.1	0.49	0.51	0.4	0.2	0.2
0.57 to 0.59	0.5	0.55	0.45	3.0	1.6	1.4
0.73 to 0.76	1.0	0.70	0.30	18.5	13.0	5.5
0.79 to 0.82	1.0	0.75	0.25	22.0	16.5	5.5
0.87 to 0.89	0.5	0.84	0.16	3.5	2.9	0.6

III-24

YHG R1

Table IVa - Pulsed Xenon Pumped Ruby Laser Analysis

Pump Band	Relative Strength	Amount to Laser Fluorescence	Amount to Heat	5750 A/cm^2			16700 A/cm^2		
				Lamp Power in Band	Lamp Power to Fluorescence	Lamp Power to Heat	Lamp Power in Band	Lamp Power to Fluorescence	Lamp Power to Heat
0.35 to 0.45	1	0.57	0.37	250	140	110	350	200	150
0.50 to 0.60	1	0.80	0.20	300	240	50	900	720	180

Table IVb - Pulsed Krypton Pumped Ruby Laser Analysis

Absorption Band	Relative Strength	Amount to Laser Fluorescence	Amount to Heat	5400 A/cm^2			15000 A/cm^2		
				Lamp Power in Band	Lamp Power to Fluorescence	Lamp Power to Heat	Lamp Power in Band	Lamp Power to Fluorescence	Lamp Power to Heat
0.35 to 0.45	1	0.57	0.37	100	57	37	200	114	86
0.50 to 0.60	1	0.20	0.20	250	200	50	200	560	140

Table IVc - Tungsten Pumped Ruby Laser Analysis

Pump Band	Relative Strength	Amount to Laser Fluorescence	Amount to Heat	228 W/cm^2		
				Lamp Power in Band	Lamp Power to Fluorescence	Lamp Power to Heat
0.35 to 0.45	1	0.57	0.37	3	1.7	1.3
0.50 to 0.60	1	0.80	0.20	10	8	2

YHG R1

Table V - Comparison of Krypton Pump Lasers

Krypton

	Nd:YAG	Nd:Glass	Nd:YLF	Ruby
f'	0.0345	0.031	0.016	0.064
f_{fluor}	0.0232	0.0199	0.0160	0.047
$f_{fluor}\eta Q$	0.00598	0.00753	0.00413	0.033
f_{heat}				
f_o	4.77	3.11	2.88	0.36
η	0.41	0.43.	0.41	0.7
Q	0.63	0.88	0.63	~1

YHG R1

4.0 PULSED AND REPETITIVELY Q-SWITCHED OPERATION

The equations describing the performance of laser
materials under various operating conditions are obtained
in this section. First single pulse operation is considered.
Finally, equations for high peak and high average power are
obtained for CW pumped repetitively Q-switched and pulsed laser
systems.

4.1 HIGH PEAK POWER - SINGLE PULSE

The peak power which can be emitted from a laser rod
is directly proportional to the maximum energy which can be
stored ($\Delta Nh\nu$) and inversely proportional to the length of
time it takes to remove this energy from the laser rod, τ.
The maximum pump pulse energy which the rod can absorb
before fracture is given in Table VII, row 3. Pre-lasing,
however, will ultimately limit the maximum usable pump
energy. Values of E_{max}, pre-lase appear in Table VII, row 8.

The maximum population inversion is proportional to
the maximum absorbed energy per pump pulse. The constant
of proportionality includes such factors as the doping level,
emission spectrum of the pump lamp and, of course, the
location of the absorption bands of the laser rod. Table V
compares the efficiency various lamps as pumps for the laser
materials. The ratio, $1/f_o$, of pump energy which becomes
1.06 micron radiation to that which becomes heat allows the
laser pulse energies (equation (18)) to be compared for the
optimum lamp/rod combination (Table V). The peak power is
determined by the time it takes the stored energy to leave

the laser resonator. This time is the decay time of the laser cavity (6),

$$\tau = \tau_{photon} = \frac{2\ell_{cav}}{cT_{opt}}$$

where ℓ_{cav} is the optical length of the laser cavity (assumed to be 50cm). The peak power is, therefore,

$$P_{\substack{single\ pulse \\ pulsed\ lamp}} = \left(\frac{T_{opt}C}{2\ell cav}\right) E_{laser} \qquad (36)$$

where,

$$E_{laser} = \begin{cases} \dfrac{\gamma}{f_o} \quad \dfrac{16\ell_{rod}\left(\dfrac{\pi}{2} - 1\right) r_o^{\,4}}{\pi^2} \quad \dfrac{\rho C}{k} \ U_{max,\,fract} & (fracture) \quad (37) \\[20pt] \dfrac{(1 + 2L)^2 ch}{L\ \ell_{rod}} \quad \dfrac{f_o}{\sigma\lambda\gamma} \quad \dfrac{1}{f_o} & (pre\text{-}lasing). \quad (38) \end{cases}$$

Values of E_{laser} are given in row 9 of Table VII.

In general, T_{opt} is a function of the single pass gain of the laser. $P_{\substack{single\ pulse \\ pulsed\ lamp}}$ appear in Table VII row 10. It has been assumed for these calculations that ℓ_{cav} = 50cm.

4.2 HIGH PEAK AND AVERAGE POWER

Two methods for obtaining both high peak <u>and</u> high
average power are possible. One method is repetitively
Q-switching and the other is pulsing the pump lamp at a
high repetition rate. In the repetitively Q switched
laser, the laser rod is pumped CW and the Q of the cavity
is interrupted at the repetition rate of the laser. For
high rep rate pulsed lamp operation, the time between pulses
is much less than the thermal time constant of the laser rod.
The average power absorbed by the laser rod will, as a result,
be high. Other thermal effects such as lensing will, con-
sequently, become important. The repetitively Q-switched
system will be considered first.

Repetitively Q-Switched Laser

The dynamics of a CW pumped, repetitively Q-switched
laser are discussed in this section. A criterion to de-
termine whether a laser material can generate a CW laser
output is discussed first. Finally, repetitively Q switched
operation is compared in those laser materials which can
operate CW.

Criterion for CW Operation

The minimum power density required for CW operation is
given by equation (40) of reference (6).

$$U_{\substack{fluor \\ thresh}} = \frac{P_{fc}}{V} = \frac{4\pi^2 h \Delta \nu \alpha c}{\lambda^3 \ell_{rod}} \tag{39}$$

where

P_{fc} is the minimum fluorescent pump power for oscillation

α is the total (including output coupling) single pass loss for the laser

$\Delta\nu$ is the fluorescent line width (Hz).

From equation (39) and equation (23) we find that

$$\frac{U_{heat\ thresh}}{f_o} = \frac{4\pi^2 h\Delta\nu\alpha c}{\lambda^3 \ell_{rod}} \qquad (40)$$

determines the rate of heat generation per unit volume at threshold. Requiring that this rate of heat generation be less than $U_{max,\ fracture}$ is equivalent to stating that a laser material will operate CW if

$$U_{heat\ thresh} = \left(\frac{4\pi^2 h\Delta\nu\alpha}{\lambda^3 \ell_{rod}}\right)\left(f_o\right) \leq U_{max,\ fracture} \qquad (41.)$$

The total single pass loss, α, can be expressed as (equation (10), reference 7)

$$\alpha = T_{opt} + L \tag{42}$$

$$\alpha = \sqrt{(2\ell_{rod})\left(\frac{P_{fc}}{A\ell_{rod}}\right)\left(\frac{\sigma\tau_{sp}}{h\nu}\right)} \tag{43}$$

where L represents the total loss other than output coupling, σ is the stimulated emission cross section for the laser line peak, and τ_{sp} is the spontaneous radiative lifetime. This equation for α can be further simplified by noting that

$$\frac{P_{fc}}{A\ell_{rod}} = U_{fluor~thresh} = \frac{U_{heat~thresh}}{f_o} \leq \frac{U_{max,~fracture}}{f_o} \tag{44}$$

and so

$$\alpha = \sqrt{(2\ell_{rod})\left(\frac{U_{heat~thresh}}{f_o}\right)\left(\frac{\sigma\tau_{sp}}{h\nu}\right)}. \tag{45}$$

Inserting equation (45) into equation (41), we find

$$U_{heat~thresh} = \frac{\pi^2 hc}{2\lambda\ell_{rod} n^4 \sigma\tau_{sp} f_o} \tag{46}$$

where

$$\frac{\pi^2 hc}{2\ell_{rod}} = 9.8 \times 10^{-24}~\text{Joule}. \tag{47}$$

Values for $U_{heat~thresh}$ have been computed and appear in Table VII, row 17.

YHG R1

Repetitively Q-Switched Laser Performance

A detailed discussion of CW pumped, Q-switched lasers is given by reference (7). Only their results will be presented in this section.

Peak Power

The peak power produced from such a system is given by equation (14) of (7) as

$$P_p = \frac{cT}{2\ell_{cav}} \, N_{max} \left[1 - \frac{1}{\Gamma} - \frac{\ell n \Gamma}{\Gamma} \right] \tag{48}$$

where T is the transmission of the output mirror,

$$\Gamma = (\beta N_{max}) \Big/ \left[(T + 2L)\left(\frac{c}{2\ell_{cav}}\right) \right] \tag{49}$$

where

L is the single pass loss (excluding output coupling)

N_{max} is the energy stored by the atoms in the upper laser state just before Q-switching

$$N_{max} = \frac{\mathcal{R}}{B} - \left(\frac{\mathcal{R}}{B} - N_F\right) e^{-B/f} \tag{50}$$

where

$\mathcal{R}$ is the effective pumping rate (power)

N_F is the energy stored just after the laser pulse has been emitted

f is the repetition rate of the Q-switch

and

B is the spontaneous decay rate from the upper laser state: $B = 1/\tau_{sp}$

$$\beta = \frac{\sigma}{A\ell_{rod}h\lambda} \tag{51}$$

$$\Gamma = \left(\frac{\beta N_{max}}{(T + 2L)}\right)\left(\frac{2\ell_{cav}}{c}\right) \cdot \tag{52}$$

The optimum output mirror transmission, T_{opt} for CW operation is given as equation (10) of reference (7)

$$T_{opt} = L\left(\sqrt{\frac{2VU_{fluor}\sigma\tau_{sp}}{Ah\nu L}} - 1\right) \tag{53}$$

This value for optimum CW output coupling differs little from the value for T_{opt} for Q-switched operation (7). It will, however, differ from the value T_{opt} for the pulsed lamp mode of operation. Values for t_{opt} are given in row 20 of Table VII.

The value of $\beta \approx 10^{12}$ and N_{max} is a large number.
Consequently, $\frac{1}{\beta} << 1$,

and so, equation (48) can be approximated as

$$P_p \approx \frac{cT_{opt}N_{max}}{2\ell_{cav}} \quad .$$ (54)

Values of P_p are computed and presented in row ω) of Table VII.
The optimum output coupling, T_{opt}, is a slowly varying
function and will be considered constant for comparison
of repetitively Q-switched laser systems. N_{max} will
suffice as a means for comparing those laser systems
that can operate CW and will be evaluated below.

P_p depends on the population of the upper laser level,
N_{max}, just prior to restoration of the Q of the laser cavity.
To first order, it is this quantity which determines whether
or not a material will make a good repetitively Q-switched
laser with available pump lamps. Equation (18) of (7) gives
N_{max} as

$$N_{max} = \mathcal{Q}\tau_{sp}(1 - e^{-1/f\tau_{sp}}) + (N_F)e^{-1/f\tau_{sp}} \quad .$$ (55)

At high rep rates $(f\tau_{sp} >> 1)$

$$N_{max} \approx \mathcal{Q}/f + \frac{N_F}{f\tau_{sp}}$$

$$N_{max} \approx \mathcal{Q}/f = U_{fluor}V/f \quad .$$ (56)

YHG R1

At low rep rates $e^{-1/f\tau_{sp}} \approx 0$ and so,

$$\boxed{N_{max} \approx \mathcal{Q}\tau_{sp}.}$$

(57)

Values of N_{max} (equation (57)) are given in Table VII row 19.

Average Power

The average repetitively Q-switched power, $\bar{P}$, is given as (equation (19) of (7)),

$$\bar{P} = \left(\frac{fT}{T + 2L}\right)(N_{max} - N_F)$$

(58)

where all the quantities have been defined above. Substituting the equation for N_{max}, into equation (39)

then

$$\bar{P} = \left(\frac{T}{T + 2L}\right)(\mathcal{Q}\tau_{sp} - N_F)\left[\left(f(1 - e^{-1/f\tau_{sp}})\right)\right].$$

(59)

The expression $\left[f(1 - e^{-1/f\tau_{sp}})\right]$ has a maximum of $1/\tau_{sp}$ as $f \to \infty$, thus

$$\bar{P} \sim \left(\frac{T}{T + 2L}\right) \cdot \left(\mathcal{Q} - \frac{N_F}{\tau_{sp}}\right) = \left(\frac{T}{T + 2L}\right)\left(U_{fluor}V - \frac{N_F}{\tau_{sp}}\right)$$

(60)

$\bar{P}$ has been computed for each of the laser materials (Table VII row 22).

At high repetition rates, $\bar{P}$ is just the CW power available from the laser (equation (9) of reference (7)). The average repetitively Q-switched power at high repetition rates is, essentially, given by the pumping rate, $\mathcal{R}$.

Pulsed Lamp - Peak Power

For the case where the lamp is pulsed at a repetition rate, f, the maximum laser output is limited by the smaller of $H_{max, \, pre-lase}$ or $H_{max, \, fracture}$ with the additional restriction that

$$\left(\begin{matrix} H_{max} \\ pre\text{-}lase \\ or \\ fracture \end{matrix} \right) \left(\frac{f}{V} \right) \leq U_{max, \, fracture} \, . \tag{61}$$

The peak power will be given by,

$$P_{pulsed} = \frac{U_{max, \, fracture} \, V}{(\text{pulse width}) \, (\text{rep rate})} \tag{62}$$

or

$$P_{pulsed} = \frac{\left(\begin{matrix} H_{max, \, fracture} \\ or \\ H_{max, \, pre-lase} \end{matrix} \right)}{f_o} \left(\frac{T_{opt} \, c}{2\ell_{cav}} \right) , \tag{63}$$

whichever is smaller.

Thus, in general H_{max} must be reduced at high repetition rates to prevent fracture. Equation (63) is evaluated in row (14) of Table VII for the laser materials.

Average Power

The average power from a pulsed lamp laser is just the energy per pulse times the repetition rate:

$$\bar{P}_{pulsed} = \left(E_{laser} \right) (f).$$ (64)

Thus

$$\bar{P}_{pulsed} = \begin{cases} \left(\dfrac{\begin{array}{c} H_{max,\ fracture} \\ or \\ H_{max,\ pre-lase} \end{array}}{f_o} \right)(f). \\[2em] \left(\dfrac{VU_{max,\ fracture}}{f_o} \right)(f) \end{cases} \text{(whichever is smaller).}$$ (65)

Values of $\bar{P}_{pulsed}$ in equation (65) are computed in row 15 of Table VII.

4.3 COMPARISON OF PULSED LAMP AND REPETITIVELY Q-SWITCHED LASERS FOR THE GENERATION OF HIGH PEAK POWER AND HIGH AVERAGE POWER

The ratio of pulsed lamp peak power and repetitively Q-switched peak power is given by

$$\frac{P_{pulsed}}{P_{repetitive}} = \frac{\left(\dfrac{U_{fluor}}{f}\right)\left(\dfrac{(1-R)c}{2\ell_{cav}}\right)}{\left(\dfrac{cT_{opt}}{2\ell_{cav}}\right)\left(\dfrac{U_{fluor}}{f}\right)} = \left(\frac{U_{fluor, pulsed}}{U_{fluor, repetitive}}\right). \quad (67)$$

As long as $(U_{fluor\ pulsed}) > (U_{fluor\ repetitive})$ pulsed lamp operation will provide higher peak powers. Since this is the case for pulsed lamps, they will yield higher peak powers up to their maximum operating repetition rate.

At low repetition rates, the pulsed lamp system will yield more average power than will the repetitively Q-switched laser. This is easily understood when one realizes that for the CW lamp laser the lamp is on all the time while the laser is emitting for a very brief period. The ratio of average powers is given approximately by

$$\frac{\bar{P}_{pulsed}}{\bar{P}_{repetitive}} = \frac{1}{\tau_{sp}f(1 - e^{-1/\tau_{sp}f})} \approx \left(\frac{1}{\tau_{sp}f}\right) \quad (68)$$

4.4   SUMMARY OF PULSED AND REPETITIVELY Q-SWITCHED OPERATION

Pulsed and repetitively Q-switched lasers each have their regions where they operate more efficiently. In general, low frequency operation is the realm of pulsed lasers for both high peak and high average power. Above the maximum repetition rate of pulsed lamps, repetitively Q-switched lasers take over.

YHG R1

5.0 COMPARISON OF LASER MATERIALS

The equations derived in the preceding sections are applied to several laser materials in this section. The results are then evaluated to determine which mode of operation best suits which material.

5.1 PHYSICAL PROPERTIES OF LASER MATERIALS

The physical properties required for the calculations which follow, are given in Table VI. Most of the values in the left half of this table have been measured. Those in the right half, however, are estimates (indicated by square brackets: [ ]). Predictions based on these values should be approached with caution.

5.2 SUMMARY OF PERTINENT EQUATIONS

Table VII serves both as a summary and as a means for comparing the laser materials. Row (1) is equation (3) evaluated for the laser materials and indicates how resistant a material is to thermal fracture. Rows (2) through (13) compare the pulsed laser capabilities while rows (14) through (20) compare the repetitively Q-switched capabilities of the laser materials considered.

A brief description of rows 2 through 20 is presented below:

ROW	CONTENTS
2	The ratio of $\left(\dfrac{\rho C}{k}\right)$ which indicates how quickly a material will respond to changes in the thermal loading
3	Equation (16) is the maximum energy the material can absorb before fracture.

TABLE VI

Physical Properties of Laser Materials

Characteristic	Nd:YAG	Nd:Glass	Ruby	Nd:YLF	Nd:BaMg Germanate	Nd:BMAG	Nd:CaZn Germanate	Nd:Bis. Germanate	Sodium Nd.Germ. Crystal	Sodium Nd:Germ. Glass
λ, wavelength (μ)	1.06[8]	1.06	0.69	1.05	1.05	1.06	1.06	1.06	1.06	1.06
k, heat conductivity (W/cm-°c) (20°C)	0.14[8]	0.0085[12]	0.37[12]	0.02[21]	[.028][18]	[.028][18]	[.028][18]	[.028][18]	0.115[23]	[.0085]
ν, Poisson's ratio	0.25[9]	0.225[13]	0.3[12]	[.25]	.25	[.25]	[.25]	[.25]	-	[.225]
σ_2, tensile strength (KPSI)	30[1]	7[26]	65[5]	15[21]	13[18]	-	20[18]	-	-	[20][13]
α_T, thermal expansion coef. (1/°c) × 10⁻⁶	6.9[8]	9.1[13]	5.8[16]	10.5[21]	10[18]	10[18]	10[18]	-	-	[9.1]
ρ, density (gm/cm³)	4.2[8]	2.2[26]	4.0	[4.0][18]	4.92[21]	4.74[21]	5.26[21]	[4]	[4][25]	[4][25]
C, specific heat (c cm-°c)	0.585[26]	0.2[26]	0.775[26]	1.85[CaF₂][3]	1.1[18]	[.1][18]	[.1][18]	[.1][18]	[.1][18]	[.2]
n, index of refraction	1.82[8]	1.50[13]	1.78[16]	1.47[18]	1.8[18]	[1.86][18]	[1.8][18]	-	1.67[25]	[1.5]
$\Delta\nu$, fluorescent linewidth (cm⁻¹)	4.2[10]	220+[13]	11	12+[28]	54+[18]	36+	54+[18]	-	270+[25]	290+[25]
t_{sp}, radiative spontaneous lifetime (μsec)	530[10]	1360	3000	-	-	-	-	-	-	1360
t_u, measured lifetime (μsec)	230[10]	585[13]	-	500[3]	320	380	320	[350]	[<8][24]	[585]
E, Young's modulus (PSI) (10⁷)	4.5[1]	1[26]	5.6[3]	[1][21]	[1][21]	[1][21]	[1][21]	[1][21]	-	[.7][21]
Q, fluorescent efficiency	0.63[11]	0.88[11]	0.7[17]	-	-	-	-	-	-	[.8]
η, quantum efficiency of upper laser level	0.5[22]	0.43[27]	0.7	-	-	-	-	-	-	-
σ, cross section (cm²) (10⁻²⁰ cm²)	50	1.4[14]	2.5[17]	10[14]	6.3	9.0	7.3	[8]	61*	1.1*

[ ] = estimate

* computed from $\nu_r = \dfrac{(n^2 \nu_{rad} \Delta\nu)_{YAG}}{(\Delta n^2 \nu_u)_x}$

* computed from $\Delta\nu(cm^{-1}) = \dfrac{\Delta\lambda(cm)}{\lambda^2_{(cm)}}$

NOTE   The spontaneous relative lifetime should be used in the denominator rather than the measured
lifetime, but values for τ_{rad} are not known at this time. The computed value is correct to
within a factor of two, however.

III-42

ROW	CONTENTS
4	The ratio $1/f_o$ from equation (23)
5	Equation (21) – the fractional amount of pump energy which can be stored due to the lifetime of the upper laser level.
6	The maximum laser output energy from thermal considerations
8	Laser energy when pre-lasing begins.
9	The smaller of $E_{max, pre-lase}$ or $E_{max, fracture}$.
10	The peak pulsed power for the laser pumping rate limited by pre-lasing or fracture (whichever is smaller).
11	The maximum absorbed pump energy per pulse before thermal fracture for the lamp pulsed at a rate f_o (average power before fracture).
12	The maximum energy of the laser pulse before fracture for a 50pps lamp pump.
13	The smaller of lines 9 or 12. This quantity represents the maximum laser energy per pulse which can be generated at 50pps.
14	The peak powers for a 50pps pulsed laser system using line 13 as the maximum laser pulse energy the rod can produce at 50pps.
15	The average pulsed power for the pulsed laser [energy per pulse (line 13) times 50pps].
16	The ratio $\dfrac{1}{n^4 \sigma \tau_{sp} \lambda}$ required for computing the CW threshold.
17	The heat loading at threshold.
18	The pumping rate of the upper laser level when the rod is pumped at its fracture limit.

ROW	CONTENTS

19   The energy stored in the population inversion just prior to Q switching when the laser rod is pumped at its fracture limit.

20   The optimum output mirror transmission when the laser rod is pumped at its fracture limit.

21   The peak power which could be obtained if the laser rod were pumped at its fracture limit.

22   The average Q-switched power when the laser rod is pumped at its fracture limit.

Table VII – Summary of Computations

Row	Equation	Equation	Nd YAG	Nd Glass	Ruby	Nd:YLF	Nd BaMGe	Nd BMAG	Nd CaZnGe	Nd bismuthGe	Nd Sodium germ, crystal	Nd Sodium germ, glass
1	3	$U_{max, fracture} = \frac{8\pi K(1-\mu)\sigma_o}{\alpha E \lambda}$ (watts/cm³)	813	39	4120	192	[336]	[336]	[336]	[336]	[336]	[165]
2	-	$\Delta r\left(\frac{1}{r_{cm}}\right)$	17.6	51.7	8.4	107	[12.5]	[17]	[19]	[14]	[3.46]	[94]
3	16	$H_{max, fracture}$	1310	166.0	32000	1890	[580]	[560]	[630]	[470]	[115]	[1425]
4	23	$U_{fluor} = U_{heat} \; \eta/\eta_o$	0.092	0.148	0.277	0.126	[1/8]	[1/8]	[1/8]	[1/8]	[1/8]	[0.148]
5	21		0.46	1	0.5	1	0.64	0.76	0.64	[0.7]	[0.016]	[0.016]
6	26	$E_{laser, max, fracture}$	55	275	4400	240	[15]	[51]	[48]	[39]	[.22]	[3.38]
8	8	$E_{laser, max, pre-lase}$	0.129	4.61	2.58	[0.213]	[1.03]	[0.715]	[0.863]	[0.806]	[0.106]	[5.80]
9	9	$E_{laser, fracture}$	0.129	4.61	2.58	[0.213]	[1.03]	[0.715]	[0.863]	[0.806]	[0.106]	[3.38]
10	34	$P_{single pulse, pulsed lamp}$	0.39	13.8	7.4	[0.65]	[3.0]	[2.16]	[2.64]	[2.43]	[0.33]	[10.2]
11		$H_{max, fracture}$	51	2.45	26	[12]	[21]	[21]	[21]	[21]	[21]	[10]
12		H_{max}	4.7	8.35	72	[1.5]	[2.6]	[2.6]	[2.6]	[2.6]	[2.6]	[1.3]
13		E_{max}	0.13	0.36	2.6	[0.21]	[1.0]	[0.72]	[0.48]	[0.8]	[0.11]	[1.3]
14	62	$P_{ave, cw}$	.39	1.04	7.8	[0.63]	[3.0]	[2.16]	[2.64]	[2.43]	[0.33]	[4.5]
15	6	P_{pk}	19.5	54	390	[31.5]	[150]	[106.0]	[132.3]	[121.5]	[16.5]	[225]
16	44		.52	9.8	1.93	[1.36]	[4.46]	[2.3]	[3.81]	-	[24.8]	[13.0]
17		$I_{heat, thresh}$	3.46	142	52.3	[12.1]	[54.6]	[21]	[45.2]	-	[304]	[188]
18	23	$I_{fluor, max}$	74.8	5.8	1160	[25]	[42]	[42]	[42]	[42]	[42]	[24.4]
19		ν_{max}	0.13	0.02	12.4	[.039]	[.042]	[.050]	[.042]	[.046]	[.00*]	[.104]
20		T_{pk}	.46	-	0.7	[1.123]	[0]	[1.0]	[0]	[1.011]	[1.00]	-
21	54	P_{v}	9	-	1250	[1.23]	-	[.52]	-	[1.345]	-	-
22	63	P	235	-	356	[78.5]	[132]	[132]	[132]	[132]	[132]	-

*These calculations are based on the thermal properties of Nd glass.

III-45

5.3 COMPARISON OF LASER PERFORMANCE

The highlights of Table VII are repeated as Table VIII.
From this table it is easy to compare the relative operating
characteristics of the laser materials.

Ruby is an excellent pulsed laser material. Unfortunately
it is not covert.

The germanates provide the best (high peak and high average
power) covert host material of those considered.

Glass is great for one giant pulse, but its poor thermal
properties limit its average power capabilities. YAG and YLF
are both poor pulsed laser materials, mainly because of their
high gains.

5.4 GERMANATE MATERIALS

The germanates appear to be ideally suited for pulsed
operation at high average powers, primarily because of their
thermal properties and energy storage (intermediate between
glass and YAG). They do not appear to have much potential as
CW sources of 1.06μ radiation because of their CW thresholds.
In short, they will provide a high peak power, high average
power covert laser source in the near IR.

Table VIII – Summary Comparison of Laser Materials

Row	Equation	Quantity	Nd:YAG	Nd Glass	Ruby	Nd:YLF	Nd:BaMgGe	Nd:BMAG	Nd:CaZnGe	Nd:BismuthGe	Sodium Nd:Germanate Crystal	Sodium Nd:Germanate Glass
1	3	U_{max} fract.	813	39	4120	192	[336]	[336]	[336]	[336]	[336]	[165]
10	38	P single pulse pulsed lamp	0.39	13.8	7.8	[0.63]	[3.0]	[2.16]	[2.64]	[2.43]	[0.33]	[10.2]
13	-	E_{50} pps	0.13	0.36	2.6	[0.21]	[1.0]	[0.72]	[0.88]	[0.81]	[0.11]	[1.5]
14	63	P_{pulsed} (>10^8) 50 pps	2.39	1.08	7.8	[0.63]	[3.0]	[2.16]	[2.64]	[2.43]	[0.33]	[4.5]
15	65	$\bar{P}_{pulsed}$	19.5	54	390	[31.5]	[150]	[108.0]	[132.0]	[121.5]	[16.5]	[225]
17	46	$U_{heat\ thresh}$	3.48	.12	52.5	[17.1]	[54.6]	[27]	[45.2]	-	[304]	[188]
20	54	P_p (×10^7)	0.46	-	0.??	[.173]	[0]	[.07]	[0]	[.051]	-	-
22	60	$\bar{P}$	235	-	3560	[78.5]	[132]	[132]	[132]	[132]	[132]	-

[ ] estimates

III-47

REFERENCES (Part III)

(1)   W. Koechner, Appl. Opt., $\underline{9}$, 1429 (1970).

(2)   L.G. DeShazer and L.G. Kamai, J. Opt. Soc. Am., 55, 940 (1965).

(3)   Thonton et al, Appl. Opt., $\underline{8}$, 1087 (1969).

(4)   W. Koechner, Laser Focus, April, 1970, p. 37.

(5)   J.L. Walsh, J.F. Asmus and A.F. Milton, "Report of Study on Optically Pumped Lasers and Non-linear Optics", Research Paper P-547.

(6)   A. Yariv and J.P. Gordon, Proc. IEEE, Jan., 1963, p. 4.

(7)   R.P. Chesler et al, "A Practical High Repetition Rate Q-switched YAG:Nd Laser, Bell Labs, Murray Hill, N.J.

(8)   Airtron Inc., Morris Plains, N.J., Product Bulletin.

(9)   J.D. Foster and L.M. Osterink, Journ. Appl. Phys., $\underline{41}$, 3656 (1970).

(10)   T. Kushida et al, Phys. Rev., $\underline{167}$, 290 (1968).

(11)   R.A. Brandewie and C.L. Telkc, J. Opt. Soc. Am., $\underline{57}$, 1221 (1967).

(12)   D.L. Flannery, "Thermal-Optic Distortion", Aug. 1970, Table II.

(13)   A.D. Baldwin and E.P. Reidel, Journ. Appl. Phys., $\underline{38}$, 2726 (1967).

(14)   QPR #1

(15)   I.J. D'Haenens and H. Evtuhov, Quantum Electronics III, Ed. by Grivet and N. Bloembergen (1964) p. 1134.

(16)   Linde Crystal Products Bulletin.

(17)   T.H. Maiman et al, Phys. Rev., 123, 1151 (1961).

(18)   Private Communication A. Linz.

REFERENCES (Continued)

(19) R.V. Alves et al, "A Lanthanium Oxysulfide Laser",
      Lockheed, Palo Alto, Research Laboratory, Palo Alto,
      California, 94304.

(20) R.A. McFarlane, "A Summary of Available Data on the
      Physical Properties of Synthetic Sapphire", Adolf
      Meller Co., Providence, R.I.

(21) Private communication, R. Folweiler.

(22) Computed from Equation (29).

(23) J. Schroder, Rev. Sci. Inst., 34, 615 (1963).

(24) E. Chicklis, private communication.

(25) Herb Lipson, private communication.

(26) C.P. Christensen et al, IEEE J.Q. Elec., QE-5, 276 (1969).

PART IV

EXPERIMENTAL EVALUATION OF
SCHOTTKY BARRIER DETECTORS

1.0 INTRODUCTION

Infrared detectors for wavelengths longer than the normal silicon sensitive region are relatively expensive and/or slow. The Air Force has substantial interest in further using longer wavelengths for purposes of covertness, safety or other purposes. Sources of radiation are becoming more plentiful in this region, and better detectors are required.

The development, at AFCRL, of a silicon device with enhanced response in the hot electron region, 1.1 to 2.2μm, is of particular interest because of the generally low cost of manufacturing silicon devices. These AFCRL detectors had been shown to have excellent high frequency response and potentially useful detection efficiency.

This program was undertaken to provide data on these detectors using lasers of different wavelengths in the band of interest, comparing the results to other available detectors. The program also developed some of the radiometric parameters that are used to characterize detectors for design purposes.

2.0 EXPERIMENTAL MEASUREMENTS

Pulsed lasers operating at three different wavelengths were used as sources of radiation, providing coverage of the most useful region of the detectors. Detectors optimized for the several wavelengths were provided by AFCRL. The data for these experiments are reported below.

2.1 Laser Measurements

2.1.1 Measurements at 1.15μm

Data was obtained utilizing a Spectra Physics Model 115 HeNe laser operating at 1.1523μm, with an output of 9.33 mW. A standard test set-up was employed with appropriate load, pre-amplifier, oscilloscope, and Wave Analyzer for signal and noise readout. (See block diagram, Fig. 1.) AFCRL Detector PdN-25 was used, at a chopping frequency of 620 Hz, to compare the detectors' sensitivity to that of known detectors.

The test data, as shown in Table 1, indicates that the AFCRL detector has a current sensitivity and quantum efficiency which is as good as, or better than, a PIN-5 Shottky barrier device. Data obtained from the manufacturer correlates reasonably close to the data obtained by Sanders Associates, Inc.

There is a possibility that the sensitivity of the AFCRL detector might be lower than indicated, since the detector area

is much smaller than the laser beam and might have been
seeing the center of the beam, thus increasing signal output.
It is felt that this difference is no more than a
factor of two.

Attempts were made at checking the detectors with a 20
nanosecond HeNe pulse, but problems with the laser prevented
the taking of reasonable data.

2.1.2 Measurements at 1.54μm

Detector measurements at 1.54 microns were made using an
Owens-Illinois ED-7 Yb-Er glass laser. The 1/4 x 3 inch rod
was mounted in a flashpumped cavity and lased in normal mode
(long pulse) operation. Figures 3 through 6 show the detector
output of an AFCRL Si Schottky barrier device operated at room
temperature. For comparison purposes, a number of shots were
taken with a Barnes A-100 InAs detector operated at room temperature.
The wiring diagram used for the InAs and Si device is
shown in Fig. 2.

Radiometric measurements were not attempted; however, the energy output per event was ~ 20 mJ and the estimated peak power in each normal mode pulse is of the order of 100 watts. The cross section of the laser pulse was 0.2 cm^2, the detector area 2×10^{-3} cm^2. Thus the peak power incident on the Schottky barrier device is roughly estimated to be 1.0 watts per individual pulse.

The observed pulse width of 22μs is believed to be characteristic of the laser emission as shorter pulses were <u>not</u> observed with the detector back biased or with the InAs. The wavelength of the emission was checked by measuring the energy output with and without inserting a narrow bandpass filter in the beam.

Given the energy falling on the detector and the output pulse, it is possible to compute relative responsivity and quantum efficiencies. These calculations, however, are not given because they would be only order of magnitude approximation because of the uncertainty in the peak power per given event.

2.1.3 Measurement at 2.06μm

The tests were made using Sanders Associates' Model 5I7 2.06μm, room temperature laser, in the single pulse mode. The AFCRL detector, PdP-2, was mounted in a copper dewar and cooled to 77°K when operated. For comparison purposes, a room temperature Philco-Ford Indium Arsenide detector was tested under the same conditions.

The detectors were placed 0.5m from a diffuse target, approximately normal to the diffuse surface. The laser was run normal mode, beamsplit into the diffuse surface. The peak power was approximately 100 watts/cm^2 illuminating an area of approximately 0.1 cm^2. Results are shown in Figs. 7-10 and test setup shown in Fig. 11

The InAs detector is a relatively low impedance device, approximately 50 ohms at room temperature unbiased, whereas the AFCRL device is in the megohm region at the operating temperature of 77°K. The active area of the InAs detector is 2 x 10^{-4} cm^2 compared with 2 x 10^{-3} cm^2 for the AFCRL device. These two factors, the device impedance and its load, plus the area difference, reasonably account for the output signals being comparable. In the InAs case we are looking at a signal across a 1KΩ load and a small active area; in the AFCRL case we are looking at the signal across a 100K ohm load and a larger area, with a back bias of 3.0 volts.

To prove this, we took both devices to AFCRL and measured their respective responsivities and from this computed quantum efficiency. The data is shown in Table 2, and indicates the difference between the two devices.

Q-Switching:

The Q-switched output of the 5I7 laser at 2.06μm was
recorded with a Philco L4530 and the AFCRL PdP-2E device
under the following conditions:

	PdP-2E	L4530
Temp:	195°K	300°K
Load Resistance:	100Ω	50Ω
Biasing:	-3V	None

The Q-switched output was approximately 15mJ with a
peak power of ∼ 0.2MW. Fig. 13a shows the output of the Philco
L4530 and Fig. 12 the output of PdP2E at ∼ 4cm from a diffuse target.
Both devices operated as indicated above exhibited voltage outputs
roughly the same under the conditions described above. Note,
however, that the pulse to pulse amplitude reproducibility of
the laser output may vary up to 50% and only crude amplitude
comparisons can be made. These photos were taken by delaying
the scope sweep by a fixed increment after the trigger pulse
to the flashlamp (∼367μs). Attempts to obtain faster sweep
times using this technique were unsuccessful as the inherent
jitter in the timing of the output pulse (∼ 2μs) prevents util-
ization of the delay mode with sweep speeds greater than 1μs/cm.

Figures 13b and 13c show the output of the L5330 with a
faster sweep speed showing the rise time of the pulse (the
frequency response of the L4530 diode is ~ 2 GHZ). These
photos were taken by triggering the scope off the input pulse.

Scope triggering for faster sweep speeds was not success-
ful with the PdP-2E due to spurious RF pulses randomly trigger-
ing the scope whose origin was the electrical discharge into
the flashlamp. These spurious pulses could not be eliminated
despite very careful shielding of the back bias circuit.

Table 1

DATA OBTAINED WITH HeNe LASER

TEST CONDITIONS

- HeNe Laser Spectra Physics Model 115
- Wavelength = 1.15μm
- Power Falling on Detector = 1.3×10^{-4} w/cm^2
- Chopping Frequency = 620 Hz

Detector	Active Area (cm^2)	R Load MΩ	Back Bias Volts	Signal mV	Noise μv	Sensitivity Amp/watt	QE %
AFCRL PdN-25e	2.03×10^{-3}	1.0	5.0	340	0.5	0.108	11.6
UDT PIN 5	3.0×10^{-4}	1.0	5.0	28	0.8	0.088	9.5

TABLE 2

DATA OBTAINED AT AFCRL ON InAs
AND AFCRL DEVICE

Test Conditions:
Source: Monochromator (calibrated)   Brower Labs Type 132 S/N Meter
Wavelength: 2.1μm   Brower Labs Type 131 Lock-in VM
Chopping Freq: 400 Hz
Power Falling on Detector: 92×10^{-6} w/cm^2

Det.	Active Area(cm^2)	R Load (Ohms)	Bias (volts)	Test Temp	Sig. μv(rms)	Resp. A/W	Q.E. %
AFCRL PdP-2E	2.03×10^{-3}	1 Meg	None	77°K	12.0	0.064×10^{-3}	.004
InAs* P-F	2.0×10^{-4}	10K	None	300°K	22.0	0.12	7.0

*NOTE: Philco Ford data on this is as follows:

QE = 25% @ λ peak
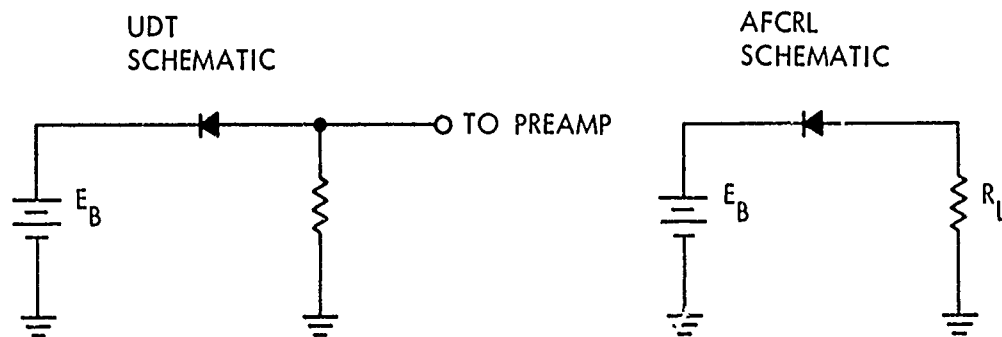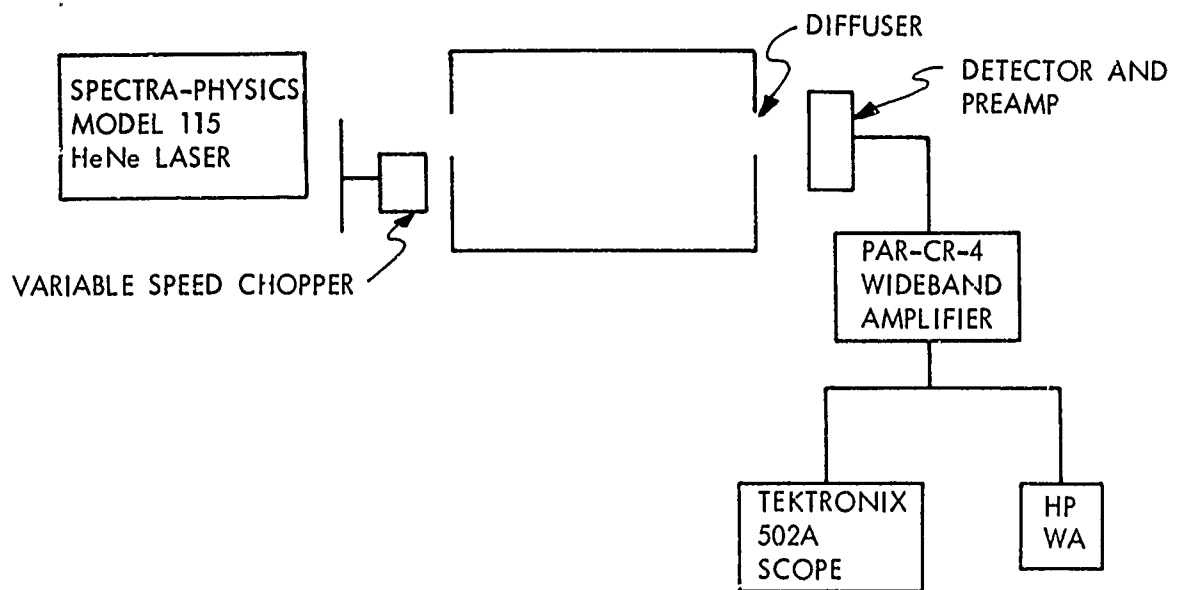
Figure 1 Block Diagram and Detector Schematics for 1.15 μm Measurement.

Er-Yb glass rod   1.54 microns

Normal Mode Operation

60 pf cable capacitance

Delay refers to time interval between initiation of flashlamp pulse
and scope trace

UNBIASED
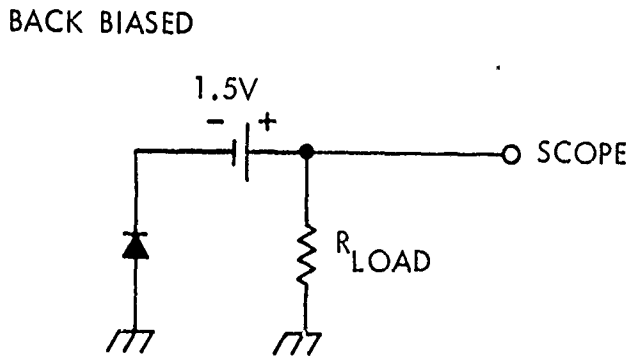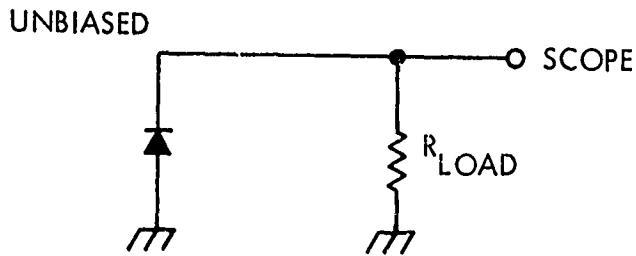
BACK BIASED

Figure 2   Experimental Setup for 1.54 μm Measurement.
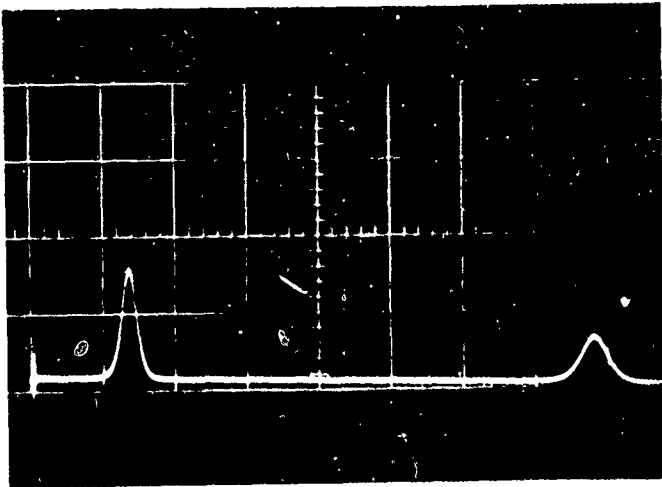
FIGURE 3

SWEEP SPEED: 5 μs/cm
DELAY: 3.5 ms
BACK BIASED DETECTOR
50 OHM TERMINATION
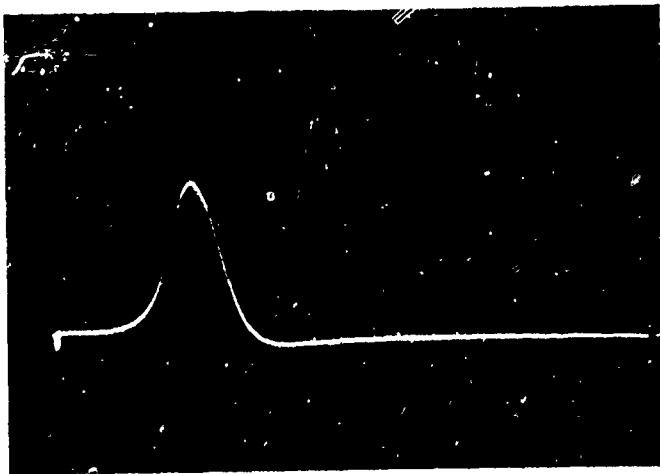
FIGURE 4

SWEEP SPEED: 2 μs/cm
DELAY: 3.5 ms
UNBIASED DETECTOR
50 KOHM TERMINATION
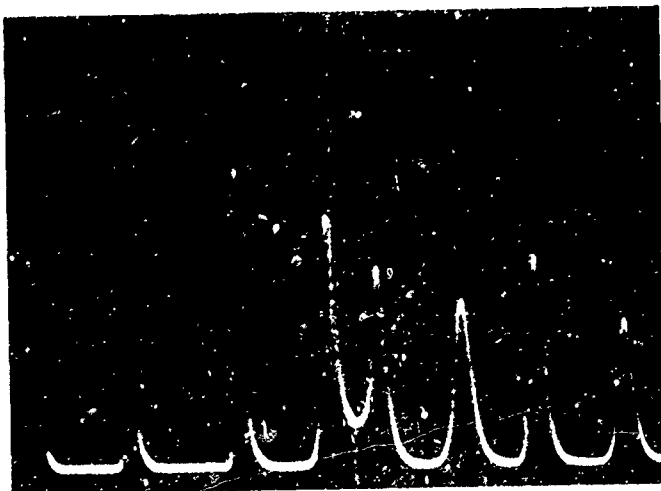
FIGURE 5

SWEEP SPEED: 20 μs/cm
DELAY: 4.0 ms
UNBIASED DETECTOR
1.0 MEGOHM TERMINATION
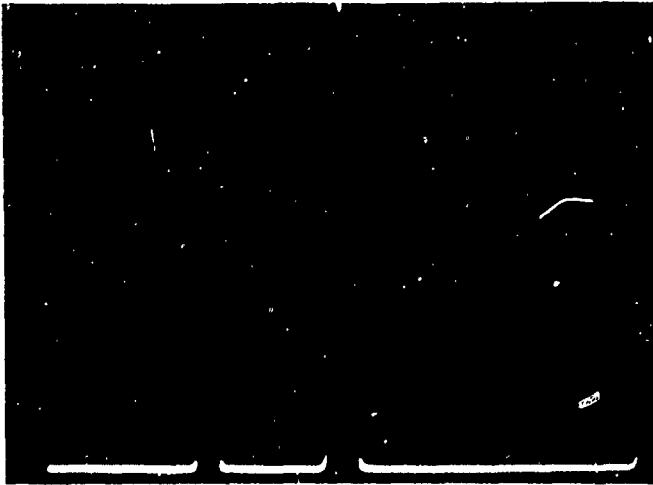
FIGURE 6

InAs
SWEEP SPEED: 20 μs/cm
DELAY: 4.0 ms
UNBIASED DETECTOR
100 OHM TERMINATION
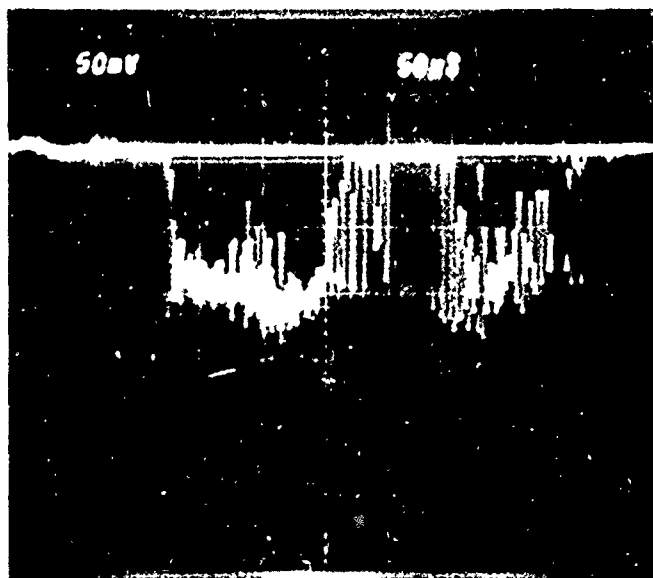
FIGURE 7

PHILCO FORD InAs @
300°K, DIFFUSE TARGET
50 mv/cm   50 μsec/cm
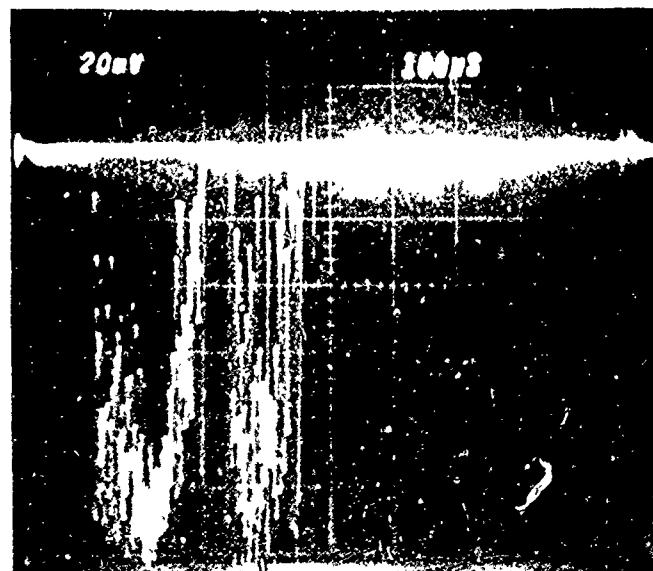
FIGURE 8

PHILCO FORD InAs @
300°K, DIFFUSE TARGET
50 mv/cm   100 μsec/cm
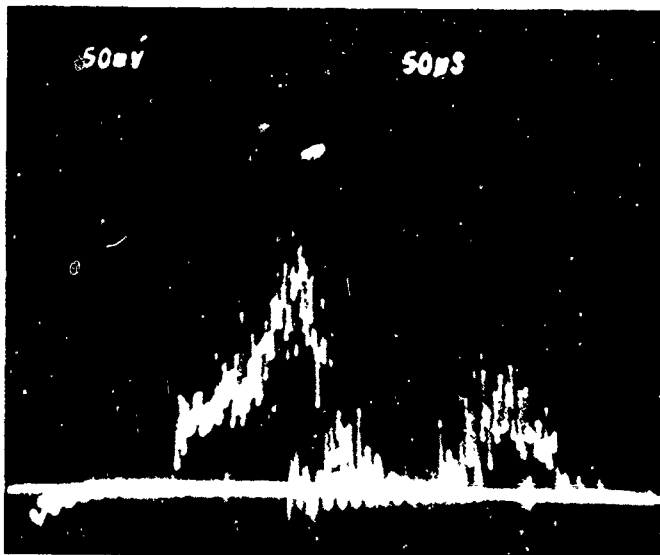
FIGURE 9

AFCRL #PdP 2E @
77° K, DIFFUSE TARGET
50 mv/cm   50 μsec/cm
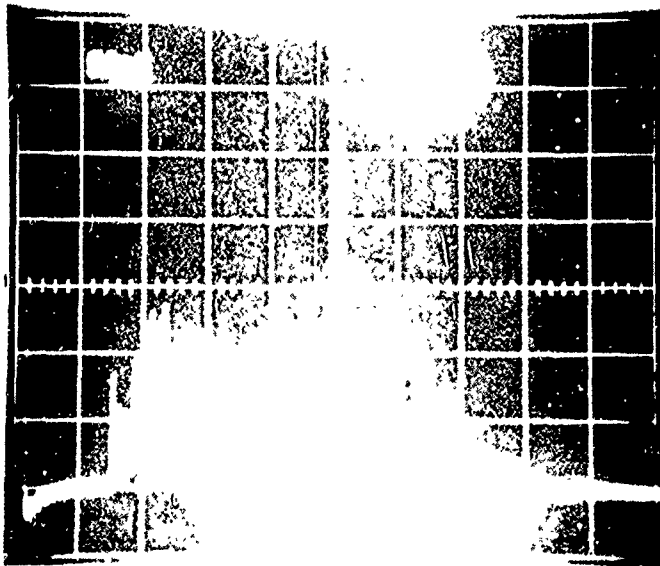
FIGURE 10

AFCRL #PdP 2E @
77° K, DIFFUSE TARGET
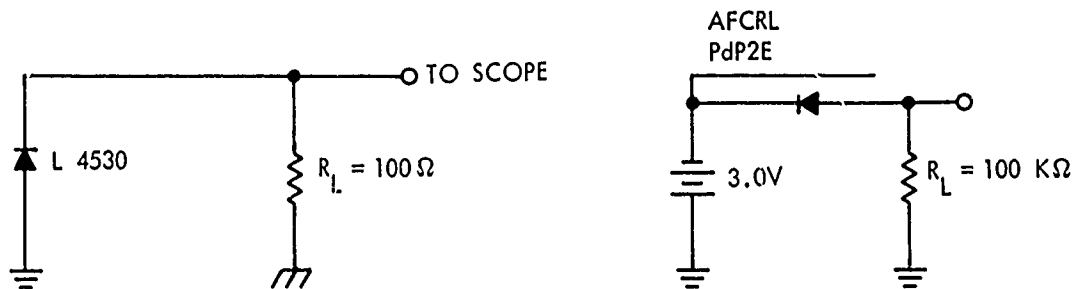50 mv/cm   50 μsec/cm

TEST SETUP:

2.06 μm NORMAL MODE

BEAM SPLITTER

DETECTOR

SCOPE   585
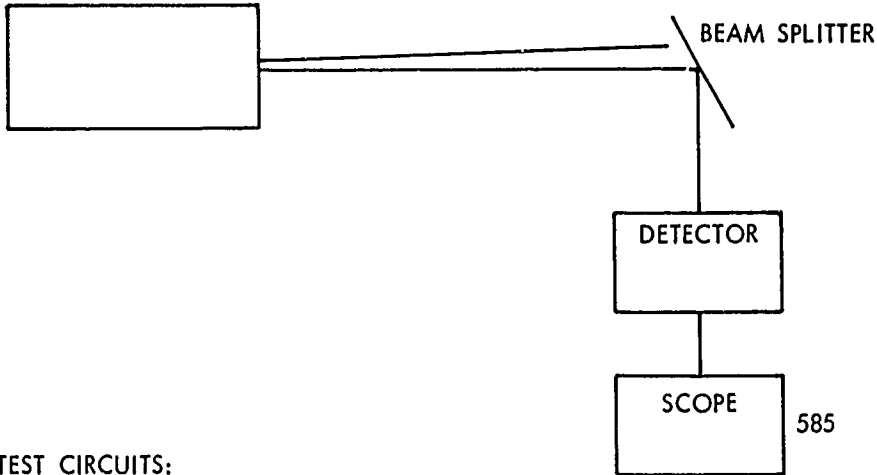
TEST CIRCUITS:

PHILCO FORD
InAs

L 4530 $R_L = 100\,\Omega$ TO SCOPE

AFCRL
PdP2E

3.0V $R_L = 100\ K\Omega$

Figure 11   2.06 μm Test Conditions.
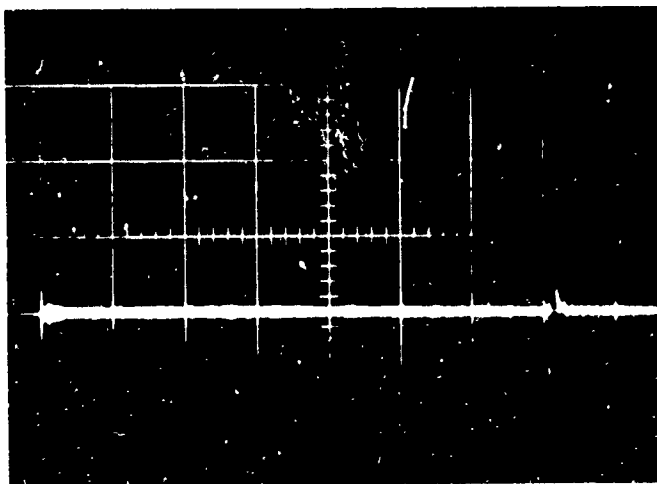
FIGURE 12
1 μsec/cm SWEEP
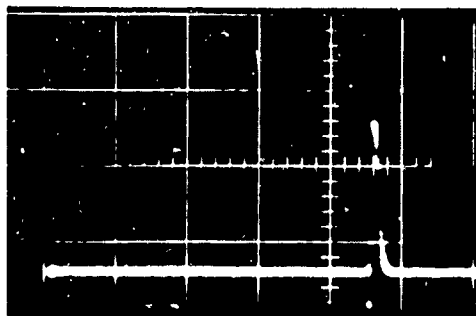
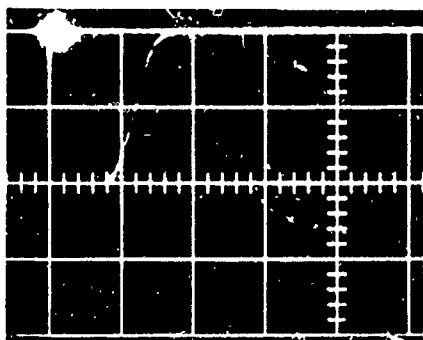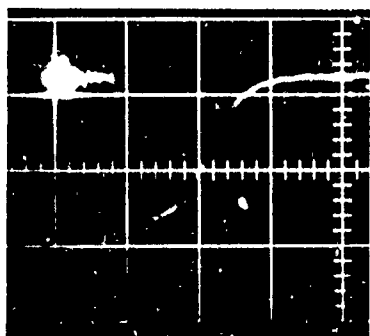FIGURE 13a

InAs
SWEEP SPEED
1 μsec/cm

FIGURE 13b

InAs
SWEEP SPEED
200 ns/cm

FIGURE 13c

InAs
SWEEP SPEED
100 ns/cm